Cognitive reserve linked to network-specific brain-ventricle coupling modes

Campo, Fulvia Francesca [1,2]; Brattico, Elvira [1,2]; Miguel, Vânia[3], Magalhães, Vicente [4]; Nigro, Salvatore [5,6]; Tafuri, Benedetta [6]; Logroscino, Giancarlo [6,7]; Cabral, Joana [3,8]*; for the Alzheimer's Disease Neuroimaging Initiative[+]

[1]Department of Education, Psychology, Communication, University of Bari Aldo Moro, Bari, Italy
[2]Center for Music in the Brain, Department of Clinical Medicine, Aarhus University & The Royal Academy of Music Aarhus/Aalborg, Aarhus, Denmark
[3]Life and Health Sciences Research Institute (ICVS), School of Medicine, University of Minho, Braga, Portugal
[4]Department of Cognitive Science, Faculty of Medicine, Faculty of Psychology, Faculty of Sciences, School of Arts and Humanities, University of Lisbon, Portugal
[5]Institute of Nanotechnology, National Research Council (CNR-NANOTEC), Italy
[6]Center for Neurodegenerative Diseases and the Aging Brain, Department of Clinical Research in Neurology, University of Bari Aldo Moro, Pia Fondazione Cardinale G. Panico, Tricase, Lecce, Italy
[7]Department of Basic Medicine, Neuroscience, and Sense Organs, University of Bari "Aldo Moro", Bari, Italy
[8]Institute for Systems and Robotics (ISR-Lisboa) and Department of Bioengineering, Instituto Superior Técnico, University of Lisbon, Portugal.

[+] Data used in preparation of this article were obtained from the Alzheimer's Disease Neuroimaging Initiative (ADNI) database (adni.loni.usc.edu). As such, the investigators within the ADNI contributed to the design and implementation of ADNI and/or provided data but did not participate in analysis or writing of this report. A complete listing of ADNI investigators can be found at: http://adni.loni.usc.edu/wp-content/uploads/how_to_apply/ADNI_Acknowledgement_List.pdf

*Corresponding author: Joana Cabral
joanacabral@med.uminho.pt
Life and Health Sciences Research Institute, School of Medicine, University of Minho, Portugal

Abstract

Despite showing significant impact in cognitive preservation, the relationship between brain activity captured with functional Magnetic Resonance Imaging (fMRI) in gray matter and ventricular cerebrospinal fluid dynamics remains poorly understood. We analyzed 599 fMRI scans from 163 elderly participants at rest with varying degrees of cognitive impairment employing a unified phase coupling analysis that breaks from convention by incorporating both tissue and ventricular signal fluctuations. This whole-brain approach identified distinct brain-ventricle coupling modes that differentiate between cognitive status groups and correlate with specific cognitive abilities.

Beyond the previously reported anti-phase coupling between global brain signals and ventricles—which we confirm occurs more frequently in cognitively normal controls—our analysis method uncovered additional coupling modes where signals in specific brain networks temporarily align with ventricle signals. At the cortical level, these modes reveal patterns corresponding to known resting-state networks: one overlapping with the Default Mode Network occurs significantly less frequently in Alzheimer's Disease patients, while another revealing the Frontoparietal Network correlates positively with memory scores.

Our findings demonstrate that different brain-ventricle coupling modes correlate with specific cognitive domains, with particular modes predicting memory, executive function, and visuospatial abilities. The coupling between signals in brain ventricles and established resting-state networks challenges our current understanding of functional network formation, suggesting an integral link with brain fluid motion. This reconceptualization of brain dynamics through the lens of fluid-tissue interactions establishes a fundamental physical basis for cognitive preservation, suggesting that therapeutic interventions targeting these interactions may prove more effective than approaches focused solely on cellular or molecular mechanisms.

1. Introduction

Healthy cognitive function, thought to emerge from the coordinated activity of billions of neurons, represents a defining trait of our species. As cognitive abilities fade, confusion expands, with many cases evolving progressively into dementia—a condition that now affects nearly 4% of people aged 65 and older, creating profound challenges for patients, families, and healthcare systems[1]. Despite decades of research, efficient therapeutic solutions for cognitive impairment remain elusive, and a reconceptualization of the fundamental mechanisms supporting healthy cognitive function is urgently needed.

Traditionally, cognitive decline has been approached from a neurodegenerative perspective, assuming that neuronal death and synaptic loss directly cause cognitive impairment. However, this relationship is more complex than initially thought—some individuals maintain cognitive function despite significant gray matter atrophy, while others experience substantial cognitive decline without corresponding structural deterioration. This suggests that additional mechanisms beyond neuronal integrity contribute to cognitive preservation or vulnerability, potentially including the dynamics of brain fluids and their interaction with neural tissue.

The relationship between brain activity captured with functional Magnetic Resonance Imaging (fMRI) in gray matter and ventricular cerebrospinal fluid inflow represents one such mechanism under active investigation [2,3]. Studies have demonstrated that the inflow of CSF in the 4th ventricle is negatively correlated with the global Blood Oxygenation Level Dependent (BOLD) signal in gray matter, a phenomenon now generally termed 'gBOLD-CSF coupling'. This coupling is particularly strong during deep sleep—a finding that has revolutionized our understanding of sleep's critical role in brain clearance mechanisms[2,4]. Despite being weaker, it is also detected during wakefulness with resting-state fMRI, where it has been shown to decrease with cognitive decline over the progression of Alzheimer's Disease[5] and Parkinson's Disease[6], challenging the conventional neurocentric paradigm. Critically, our current understanding remains limited to this single mode of brain-ventricle coupling ('gBOLD-CSF'), while the existence and potential significance of more complex brain-ventricle coupling modes for cognitive function remains entirely unexplored.

Despite occurring in the same ultra-slow frequency range (below 0.1 Hz)[7], the relationship between brain clearance mechanisms and resting-state brain activity remains poorly understood. Indeed, while cognition has been shown to systematically decline as brain-ventricle coupling weakens, the specific mechanisms linking these ultra-slow pulsations to cognitive processes are still unclear. Some evidence indicates the involvement of non-neuronal physiological processes in the organization of functional networks supporting cognitive function, but whether these are attributed solely to cardiac and respiratory rhythms, or whether additional players interact at these ultra-slow frequencies remains unclear[8]. For instance, recent studies in rodents demonstrate that optogenetically-induced neuronal activity drives self-propagating ionic waves through the cerebral fluid across the cortical tissue[7], yet how these waves organize at the macroscale and relate to the long-range correlations detected with fMRI at rest remains uncertain[8–10]. This gap in understanding highlights the need to explore more complex coupling patterns beyond the global anti-phase relationship.

Most resting-state fMRI research has focused exclusively on signal fluctuations in cortical and subcortical gray matter, identifying consistent modes of functional connectivity altered in cognitive impairment[11–13]. In a previous study, the Global Mode—where signals from all brain areas slowly co-vary together—was found to be most distinctive of cognitive performance[14].

Yet other network configurations, where some brain regions temporarily shift from the rest of the brain and synchronize together, have also been identified.

In mild cognitive impairment and dementia, decreased functional connectivity in the Default Mode Network (DMN) is particularly well-documented [15–21]. This network primarily comprises the medial prefrontal cortex, posterior cingulate cortex, precuneus, and angular gyrus, which show reduced connectivity as cognitive function declines. Other networks, such as the Salience Network[19,22,23] and Central Executive Network[24–27], also show alterations with cognitive decline.

Numerous subcortical structures—including the thalamus, basal forebrain, amygdala, hippocampus, and cerebellar regions—have been shown to either correlate with or modulate the Default Mode Network[28–36], with many showing altered functional connectivity in cognitive decline and memory loss[37–40]. However, the close proximity of these structures to brain ventricles presents a methodological challenge, as ventricular enlargement in aging makes it difficult to determine whether observed signal changes originate from neural activity or from non-neuronal contributors such as fluid inflow in the adjacent ventricular spaces or subtle spatial displacements due to physiological motion, particularly noticeable at the location of fluid-tissue interfaces.

Traditional neuroimaging approaches have typically treated fluctuations in ventricular CSF signals as confounds to be removed, potentially discarding valuable information about the physiological mechanisms supporting healthy cognitive function. This conventional approach constrains our understanding by attributing all brain activity to neurons while dismissing other sources of signal fluctuations, including fluid motion, as mere confounds. Under that viewpoint, current computational models aiming at explaining wave patterns captured at spatial scales a billion times larger than neurons are interpreted as neuronal excitability waves[10] propagating through the network of axonal connections[41]. Yet, the scenario that the globally correlated ultra-slow fluctuations in the rsfMRI EPI signal are driven by the synchronized firing of neurons raises some doubts, not only because these waves last more than 10 seconds per cycle, but also because keeping this global firing activity may not be the most efficient from an energetic perspective. At the end of the day, we need to understand the nature, the organizing principles and role of functional networks in the first place, and how they can be modulated to enhance network function or neuroprotection remains elusive.

In this study, we analyze brain activity from the Alzheimer's Disease Neuroimaging Initiative (ADNI 2) repository containing 599 resting-state fMRI recordings from clinically-evaluated elderly individuals, categorized across the spectrum of cognitive decline as early Mild Cognitive Impairment (EMCI), late Mild Cognitive Impairment (LMCI), and Alzheimer's Disease (AD), together with matched cognitively normal (CN) controls[42]. Avoiding any assumption regarding the origin of the fluctuations in fMRI signals, we minimally preprocessed the raw data without removing physiological components. We use the term 'brain-ventricle' rather than 'BOLD-CSF' coupling to acknowledge that the only differentiating factor between the fMRI signals is their anatomical location, not their underlying mechanisms.

We develop a new analysis method that searches for modes of phase coupling across the entire brain, extending the Leading Eigenvector Dynamics Analysis (LEiDA) algorithm[14,41] beyond gray matter alone. By exploring the relationship between the dynamics captured with fMRI in brain ventricles and resting-state activity in gray matter, we aim to reveal new insights into the origin of ultra-slow modes of brain connectivity detected in the resting state. Our findings point to an underexplored physical basis for cognitive function through reciprocal tissue-fluid coupling, potentially explaining why traditional drug trials targeting neuronal mechanisms alone have largely failed to combat cognitive decline, and suggesting novel therapeutic avenues targeting fluid dynamics could be more effective for preserving cognitive health.

2. Results

2.1. Mode occupancy changes with AD progression

Our analysis - oblivious of signal origin or anatomical location - revealed a set of phase coupling modes in fMRI signals that occurred recurrently over time and across scans, irrespective of the participants' condition. Despite the low spatial resolution of T2* weighted Echo-Planar Imaging (EPI) images, and the additional spatial blurring due to the realignment of 599 scans from elderly participants, the spatial maps characteristic of each mode clearly revealed a dephasing of signals in structures both with the shape and at the location of different brain ventricles. Moreover, additional spatial modes of phase orientation revealed dephasing of voxels in cortical structures. We explored the repertoire of modes obtained when clustering the data into a varying number of clusters K and report, in **Figure 1,** the modes obtained for K=4 clusters, which is representative of the results obtained across the entire range of K explored (the impact of varying from K will be described below).

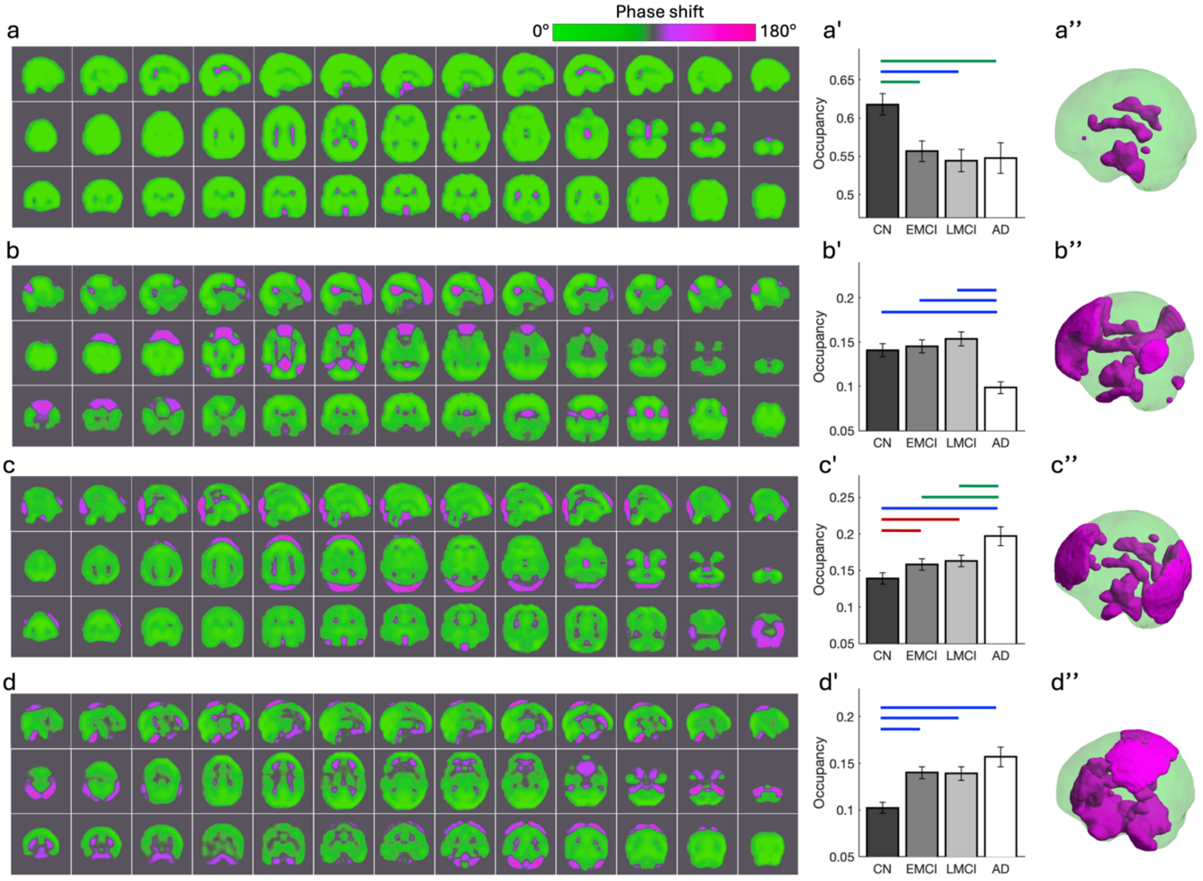

Figure 1. Four distinct phase coupling modes detected recurrently in fMRI scans and corresponding occupancy across cognitive status groups. Our approach focuses on modes of phase alignment in fMRI signals irrespective of anatomical location. The 81707 maps of phase alignment detected at each time point in s=599 scans were clustered into K=4 clusters and their occupancy calculated for each scan (see Methods for details). **(a-d)** The K=4 cluster centroids represent phase

coupling modes detected recurrently in the entire sample, where voxels colored in light green are aligned with the global signal direction, while voxels in magenta vary with a phase shift larger than 90° with respect to the global signal. Each coupling mode is shown in sagittal (top), axial (middle), and coronal (bottom) equidistant slices. (**a'-d'**) The proportion of time points during which a mode is dominant, or *Occupancy*, was calculated for each scan and compared across conditions. Error bars report the mean ± the standard error of the mean (SEM) across scans in each condition. Statistical significance was determined using non-parametric testing with 10000 permutations. *Red* bars indicates $p_{perm}<0.05$; *green* corresponds to $p_{perm}<0.05/4$ correcting for the K=4 modes compared, and blue corresponds to $p_{perm}<0.00024$ correcting by all comparisons across the full repertoire of modes obtained with K from 2 to 20, indicating a strong chance of a true positive. (**a''-d''**) The phase coupling modes are rendered in 3D, showing in magenta the smaller subset of regions shifting by more than 90° from the rest of the brain (green).

Visualizing the phase coupling modes obtained for K=4 in sagittal, axial and coronal slices (**Figure 1 a-d**) reveals distinct patterns of fMRI signal phase relationships across the entire brain, involving brain structures extending beyond gray matter, and with clear anti-phase relationships to the ventricles. The modes are characterized by the way the phase of the fMRI signals is organized, such that all the voxels colored in green covary together in phase (*i.e.*, with a phase shift <90° with respect to the collective phase orientation), while the voxels colored in magenta vary in anti-phase (*i.e.,* with a phase shift >90°) with respect to the phase of voxels colored in green.

The *occupancy* of each mode - *i.e.*, the proportion of time instants in which a mode is detected during a scan - was calculated for each scan and compared across conditions (157 scans from CN controls, 189 from ECMI, 147 from LMCI and 106 from AD patients). The 4 coupling modes detected with K=4 varied significantly in occupancy across the progression of cognitive decline and a summary of the statistical analysis is reported in **Figure 1 a'-d'**.

The first phase coupling mode (**Figure 1a**) was detected around 61.77%± 1.41% of the time in fMRI scans in CN (mean ± standard error of the mean, SEM), and occurred significantly less in all other 3 conditions, namely EMCI (55.67% ±1.34, $p_{perm}=0.0010$, Hedge's g=0.34), LMCI (54.43% ±1.46, $p_{perm}=0.00012$, g=0.42), and AD (54.76% ± 2.01, $p_{perm}=0.0020$, g=0.73). Both EMCI, LMCI and AD exhibited similar occupancy of this mode, $p_{perm}>0.25$). This mode corresponds to an activity pattern where the fMRI signals in voxels colored in magenta - around the 2 lateral ventricles and the 3rd and 4rth ventricles - vary with a phase shift larger than 90° with respect to the rest of the brain.

The second coupling mode (**Figure 1b**) was found to strongly decrease its occupancy in AD, being detected on average 9.86 ± 0.67 of the time in fMRI scans from AD patients, while in CN it occurred 14.08% ± 0.76 ($p_{perm}=0.000070$, g=0.49), in EMCI 14.51% ± 0.73 ($p_{perm}=0.000010$, g=0.51) and in LMCI 15.36% ± 0.79 ($p_{perm}=0.00000011$, g=0.64). In this mode, the voxels shifting in phase with respect to the rest of the brain (colored in magenta) extend beyond the ventricles, revealing large brain areas where the signals dephase from the global fMRI signal (these brain areas are characterized in more detail in the following sections).

The two other phase coupling modes obtained with K=4 were found to increase their occurrence over the progression of AD. BraVe Mode III (**Figure 1c**), detected around 13.90% ± 0.80 of the time in CN, was found to increase to 15.81% ± 0.78 in EMCI (p_{perm}=0.046I , g=0.18), to 16.29% ± 0.81 in LMCI ($p_{perm}= 0.019$, g=0.24 CN vs LMCI) and to 19.68% ± 1.29 in AD patients ($p_{perm}=0.000039$, g=0.51 CN vs AD; $p_{perm}=0.0045$, g=0.33 EMCI to AD; $p_{perm}=0.012$, g=0.30 LMCI to AD). Similarly to the other coupling modes, no differences were detected between EMCI and LMCI ($p_{perm}>0.20$).

The 4th coupling mode (**Figure 1d**) also significantly distinguished CN from all other groups, indicating that, similar to BraVe mode I, it becomes altered in the first stages of the disease. While occurring only 10.24% ± 0.60 in CN, it was detected 14.01% ± 0.63 of the time in EMCI (p_{perm}=0.0000093, g=0.45), 13.91% ± 0.73 in LMCI (p_{perm}=0.00012, g=0.45), and 15.70% ± 1.05 of the time in AD (p_{perm}=0.000000013, g=0.61). Similarly to mode II, the patterns of phase coupling observed in modes III and IV reveal distinct brain areas whose signals shift out of phase from the global brain signal (green) and align with the activity inside the ventricles (magenta).

2.2. Consistent modes of signal dephasing between brain and ventricles

We extended our analysis to the entire repertoire of phase coupling modes obtained when varying the number of clusters K between K=2 to K=20, given that the process of determining the optimal number of clusters in k-means clustering is inherently subjective, and different evaluation metrics like silhouette scores and Dunn's index may suggest optimal values that might not capture the most meaningful grouping for distinguishing across conditions. Despite the apparent complexity of patterns detected, they all share one particular property: the ventricles are consistently found within the group of voxels whose signals evolve in opposite direction from the majority of voxels in the brain (rendered in magenta in **Figure 2a).** Moreover, for all partitions into K clusters, the most frequently detected cluster (c=1, first column in **Figure 2a**) corresponds to the mode of 'gBOLD-CSF' coupling where the fMRI signals in the ventricles are dephased from the rest of the brain. In agreement with previous studies, this global 'brain vs. ventricles' mode (BraVe mode I) was found to decrease significantly in AD for K=2, but this change becomes less significant as the number of clusters increases, and more complex Brain-Ventricle (BraVe) coupling modes are extracted from the data.

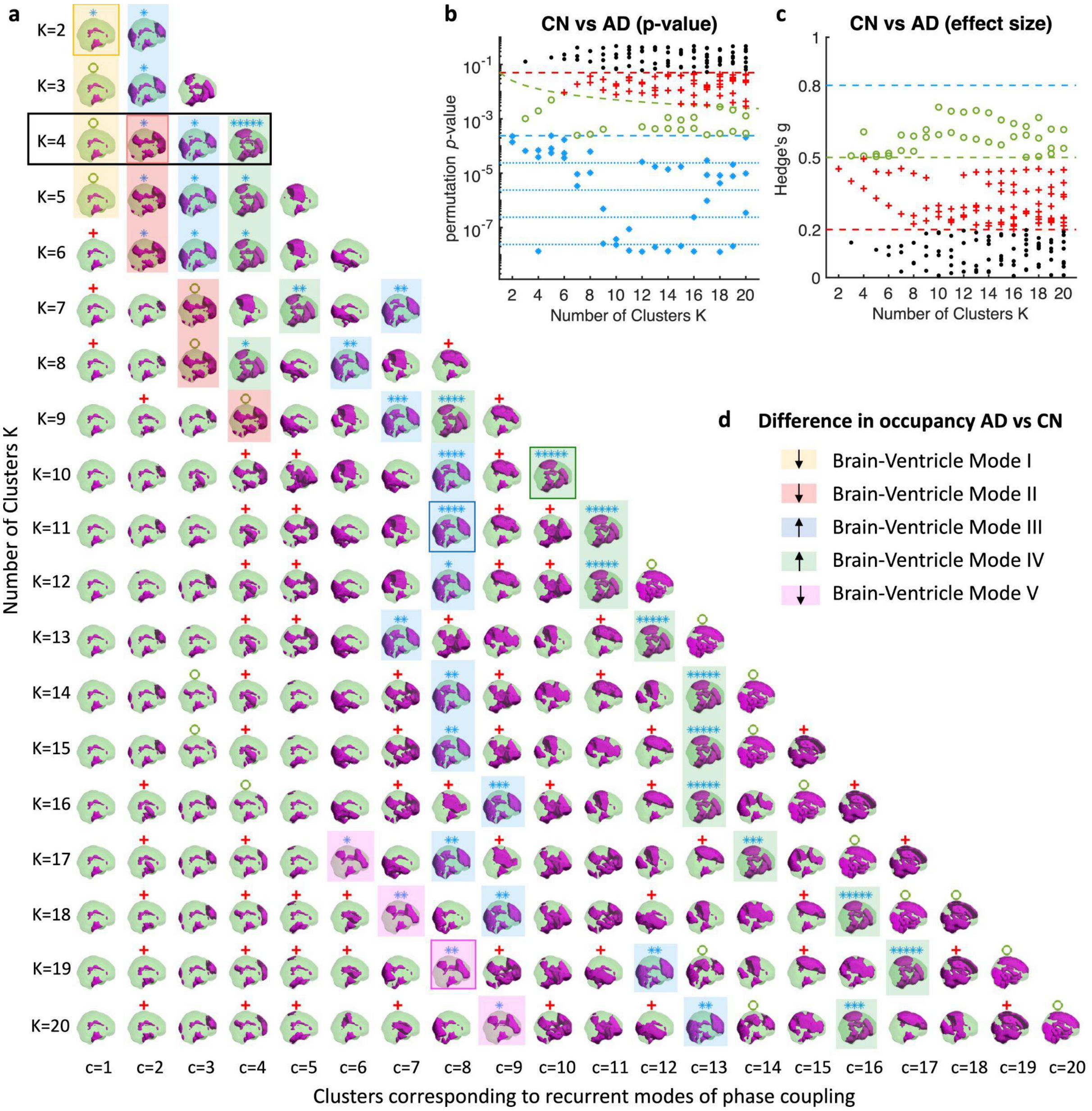

Figure 2 - Consistent Brain-Ventricle (BraVe) Coupling Modes occurring differently in AD. a. Pyramid showing all the phase coupling modes detected when varying the number of clusters (K) from 2 to 20, sorted from left to right according to their average occupancy in controls, and highlighting the ones that statistically occurred differently in AD vs CN. Each mode is represented by the corresponding cluster centroid (c) shown in a transparent brain viewed from the side, rendering in magenta all voxels whose fMRI signals are dephased by more than 90° relative to the rest of the brain. The markers on top of each mode represent the level of statistical significance (shown in **b**) comparing occupancies in AD vs CN. Symbols/colors indicate the level of statistical significance: red for $p_{perm} < 0.05$; green for $p_{perm} < 0.05/K$ accounting for K independent comparisons; and blue asterisks for $p_{perm} < 0.05/\sum_{K=2}^{20}(K) = 0.00024$, correcting for both independent and dependent comparisons across the full set of modes compared. The most significant findings are highlighted with more than 1 asterisk, where each additional asterisk represents a power of 10 relative to the stringent Bonferroni correction. **d**. Grouping the 209 modes extracted from the data, 5 spatially distinct BraVe modes were found to differentiate AD from CN scans. BraVe modes I, II and V (indicated by yellow, red and purple shades) occur more in CN, while BraVe modes III and IV (indicated by blue and green shades) occur more often in AD. Outlined boxes indicate the cluster from each mode that differentiated across conditions with the largest effect size (shown in **Figure 3**).

A substantial portion of these BraVe coupling modes (44 out of 209, ~21%) was found to differ significantly in occupancy between CN and AD (surviving conservative Bonferroni correction for multiple comparisons and with medium-to-large effect sizes, see **Figure 2 c-d**). Given that some of the clusters detected across K share strong spatial similarities, we compared the 44 cluster centroids differentiating between CN and AD (Bonferroni-corrected) and grouped them into 5 modes of phase coupling according to their spatial similarity (Pearson's $r>0.85$, **Supplementary Figure S9**). Within these 5 modes (c.f. legend in **Figure 2 d**), the first 4 correspond to the same modes detected with K=4 reported previously**.** Apart from these, a 5th mode, detected for K≥17, was found to decrease significantly in AD. This extended analysis reveals that differences between conditions may be detected at different levels of granularity, justifying the analysis across a broad range of K instead of focusing on a specific number of clusters, as long as the statistical results are adequately corrected to account for false positives arising from multiple comparisons.

Although most differences were detected between the CN and AD groups, some of these changes show larger effect sizes in specific transitions between cognitive stages (**Figure 3**). On one side, the first stages of cognitive impairment are characterized by a decreased detection of BraVe mode I (the global one) accompanied by an increased occupancy of BraVe mode IV (with signal dephasing in ventricles together with ventral and dorsal areas). As can be seen in **Figure 3**, these changes are only statistically significant (black horizontal lines for Bonferroni-corrected differences) between CN and all 3 other groups and do not change in the transition from MCI to AD. Conversely, the decreased occupancy of BraVe modes II and V is associated with the final transition to dementia, given that the occupancy of these modes was significantly decreased compared to all other cognitive stages Finally, the increase in BraVe mode III occurs more progressively, with subtle increases between cognitive stages, but only surviving Bonferroni correction between CN and AD. The final transition to dementia (from LMCI to AD) is marked by a decline in BraVe modes II and V (with signal dephasing in frontal and parietal areas) and an increase in BraVe mode III (dephasing in frontal and posterior areas. Only EMCI and LMCI could not be significantly distinguished based on mode occurrence when considering Bonferroni FWER correction. All statistical analyses between condition pairs are reported in **Supplementary Figures S1 to S8**.

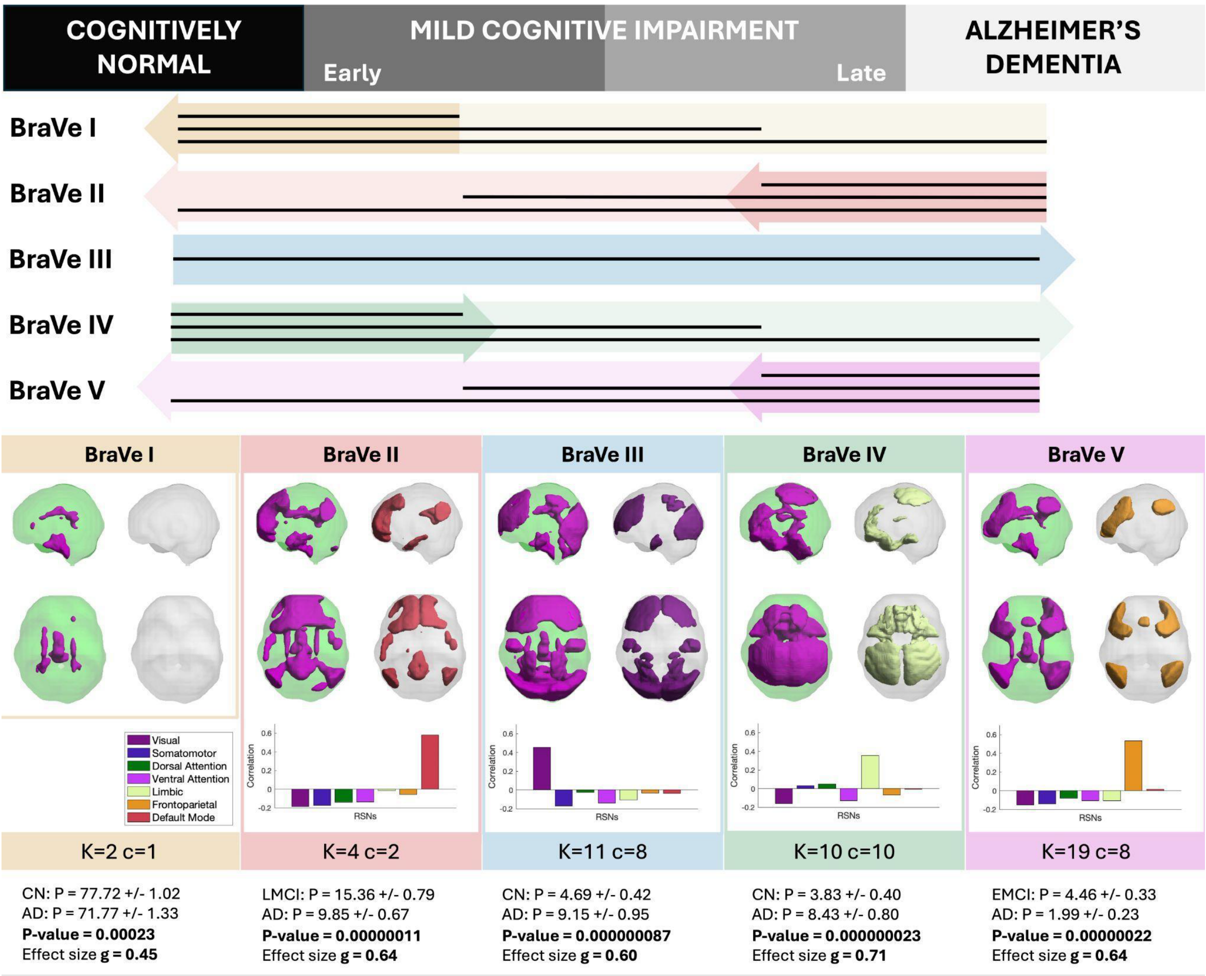

Figure 3. Occupancy of Brain-Ventricle (BraVe) modes between cognitive stages and overlap with Resting-State Networks. Top: The color-shaded arrows indicate how the occupancy of the five BraVe modes changes over the progression of cognitive decline. Two modes show statistically significant differences (black horizontal lines) between CN and EMCI participants: BraVe mode I, higher in CN than EMCI, and BraVe mode IV, higher in EMCI than CN. Two other modes differ between LMCI to AD, namely BraVe modes II and V, both higher in LMCI than AD. **Bottom**: Each of the five BraVe modes is represented by the cluster centroid that exhibited the highest effect size when comparing occupancies between any pair of conditions. Each of these 5 centroids is rendered in 3D in two distinct forms, shown in side and top views: (left) the voxels dephasing from the global phase are rendered in magenta, as in previous figures; (right) only voxels belonging to cortical areas are shown and colored according to the RSN with strongest spatial correlation, as indicated by the colored bar plots below (reference RSNs from Yeo et al, 2011). The occupancy (P, mean +/- standard error of the mean) of each mode is reported for the pair of conditions that exhibited differences with the highest effect size (Hedge's g).

Although our results were robust for most of the range of K explored, different partitions result in more significant p-values and higher effect sizes for each mode. While BraVe mode I had the highest effect size when clustering into K=2 clusters (CN vs AD, g=0.45, p_{corr}=0.048) this coarser partition into only 2 modes failed to reveal more complex modes of coupling. The partition into K=4 clusters distinguished LMCI and AD in terms of mode II occupancy with higher effect size (g=0.64, p_{perm}=0.00000011, p_{corr}=0.000022), and the partition into K=11 clusters distinguished CN from AD in terms of BraVe mode III (c=8) occupancy with g=0.60 and p_{perm}=0.000000087 (p_{corr}=0.000018). The highest effect size in this study was detected with K=10, in the occurrence of BraVe mode IV (c=10) differentiating CN from AD participants with g=0.71 and p_{perm}=0.000000023 (p_{corr}=0.0000048). Moreover, the significant decrease of BraVe mode V was detected only for finer grained partitions (K>17, being most significant for K=19, c=8). This mode strongly distinguished AD patients not just from CN (p_{perm}=0.00000078, p_{corr}=0.00016 g=0.52), but also from EMCI (p_{perm}=0.00000022, p_{corr}=0.000046, g=64) and LMCI (p_{perm}=0.000000021, p_{corr}=0.0000044, g=0.57). These highly significant p-values (four orders of magnitude smaller than the threshold for Bonferroni correction of 0.00024) with medium-to-high effect sizes indicates that these modes of brain-ventricle coupling are likely implicated in cognitive preservation.

2.3. Brain-Ventricle coupling modes reveal Resting-state Networks

Our results indicate the existence of functionally relevant modes of coupling extending beyond the dephasing of global brain signals from the ventricles (here referred to as BraVe mode I). Given that the brain areas in which the signals temporarily dephase from the rest of the brain in modes II to V form a network with correlated activity at the cortical level, we turn to investigate how the BraVe modes detected relate with canonical resting-state networks. To do so, we calculated the spatial overlap between the set of dephasing voxels located in the cortex alone and the seven resting-state networks from a widely-used template [43], defined on the same cortical voxels.

Our analysis reveals that the BraVe modes detected herein shape functional networks at the cortical level exhibiting a spatial overlap (Pearson's correlation r>=0.35) with some of the RSNs used as reference (**Figure 3 bottom)**. Namely, BraVe mode II, detected less frequently in AD patients, overlaps strongly with the DMN (red, r=0.60, shown in detail in top left). Overlapping the cluster centroids with the AAL2 parcellation into 120 anatomical cortical and subcortical gray matter areas, reveals that the voxels aligning in phase with the ventricle signals in BraVe mode II correspond to brain areas known to belong to the DMN, with most voxels in the Superior Frontal gyri, the Angular gyri, the Anterior and Posterior Cingulate gyri, the Medial Orbital Frontal cortex, and even some voxels in Inferior and Middle Temporal gyri (all including left and right parcels). A complete list of AAL2 brain areas for each BraVe mode can be found in **Supplementary Figure S10.**

BraVe mode V, occurring less frequently in AD patients, shows a strong overlap with the lateral Fronto-Parietal Network (yellow, r=0.56), including the left and right Middle Frontal gyri, Angular gyri and Inferior Parietal lobules. Although BraVe Mode III exhibits some overlap with the visual network, the correlation is lower (r=0.45) because, although most voxels are located in the occipital cortex (including the inferior, middle, and superior regions), it also includes voxels located in the frontal cortex (including the superior, middle, and inferior regions). Other voxels are found in the cerebellum, the middle and inferior temporal gyri and the lateral occipitotemporal gyrus, covering the lingual and fusiform gyri and the calcarine fissure. BraVe mode IV exhibits some overlap with the limbic network (r=0.35), with voxels being distributed in temporal regions (such as the superior and middle temporal pole, middle and inferior temporal gyrus, and fusiform gyrus) and parietal areas (including the superior parietal gyrus, inferior parietal lobule, angular gyrus, and precuneus). The cerebellum also contains a significant number of voxels, spanning several lobules. Additional voxels are present in frontal regions, including the superior, middle, and inferior frontal gyri, the anterior, medial, and posterior orbital cortex, and the gyrus rectus. The lower overlap of modes III and IV suggest that these modes that appear more often with cognitive decline do not have a direct correspondence with RSNs determined from cognitively normal and generally younger participants.

In **Figure 4**, we color the modes of phase coupling exhibiting an overlap (Pearson's correlation >0.35) with 7 resting state networks used as reference.

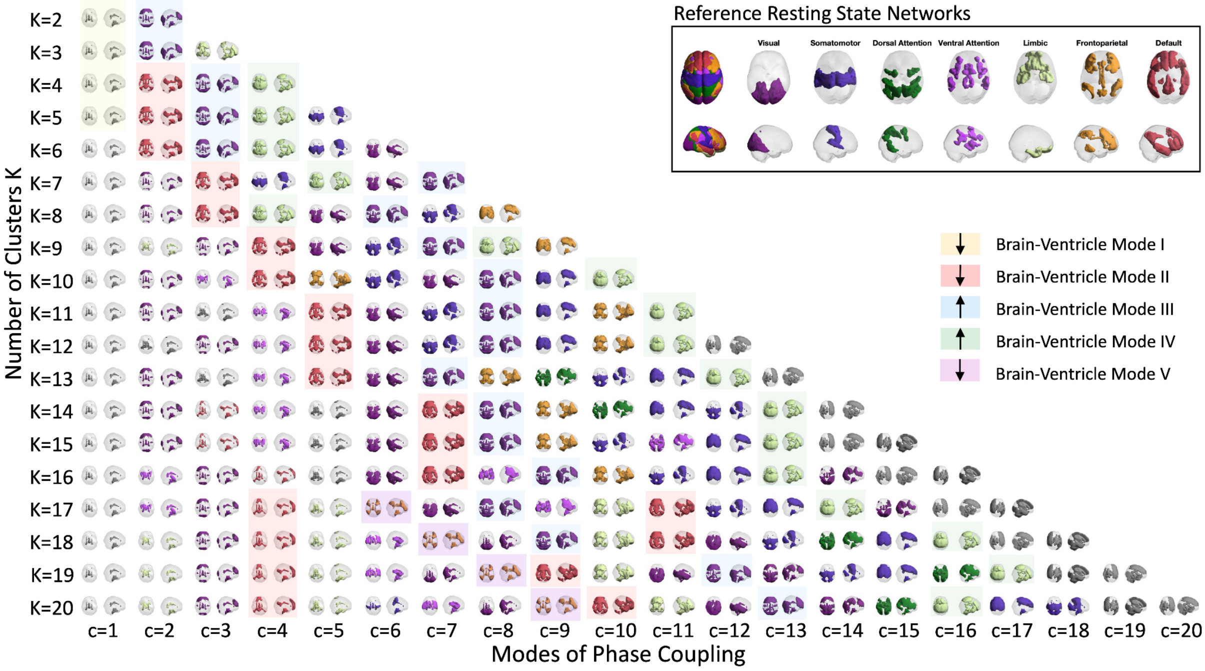
Reference Resting State Networks
Visual
Somatomotor
Dorsal Attention
Ventral Attention
Limbic
Frontoparietal
Default
↓ Brain-Ventricle Mode I
↓ Brain-Ventricle Mode II
↑ Brain-Ventricle Mode III
↑ Brain-Ventricle Mode IV
↓ Brain-Ventricle Mode V
Number of Clusters K
K=2
K=3
K=4
K=5
K=6
K=7
K=8
K=9
K=10
K=11
K=12
K=13
K=14
K=15
K=16
K=17
K=18
K=19
K=20
c=1
c=2
c=3
c=4
c=5
c=6
c=7
c=8
c=9
c=10
c=11
c=12
c=13
c=14
c=15
c=16
c=17
c=18
c=19
c=20
Modes of Phase Coupling

Figure 4. Some Brain-Ventricle (BraVe) coupling modes reveal resting state networks. Pyramid showing all the phase coupling modes detected with K from 2 to 20, highlighting in different colors all voxels whose fMRI signals are phase-shifted by more than 90° relative to the rest of the brain. The colors correspond to the resting-state networks from the template defined in [43]: red for the Default Mode Network (DMN), purple for the visual network, blue for the somatomotor network, green for the dorsal attention network, light purple for the ventral attention network, light green for the limbic network, and yellow for the frontoparietal network (FPN). Networks in gray do not correlate >0.2 with any of the reference networks. The colored shades (yellow for mode I, red for mode II, purple for mode III, green for mode IV, purple for mode V) highlight variations of the same modes as the number of clusters varies.

2.4 Brain activity as a temporal sequence of Brain-Ventricle coupling modes

To gain a better understanding of brain activity captured with fMRI, we analyze a brain scan from a CN control participant who had a high occupancy of BraVe mode 2. **Figure 5a** shows the fMRI signals over time (with Time of Repetition, TR=3 seconds), with colors in the background indicating the dominant mode (based on the cluster assignment obtained with K=4) at each instant of time, such that brain activity over an entire scan can be represented as a temporal sequence of modes. As can be seen, BraVe modes I and II are more frequently detected than Modes III and IV during this scan.

As illustrated in **Figure 5b**, an occurrence of mode II corresponds to periods of time when the fMRI signals in certain brain voxels either co-increase (red) or co-decrease (blue) with respect to the mean. Although the instantaneous snapshots of fMRI signals are very noisy, the pattern associated with BraVe Mode II (overlapping with the DMN) is clearly visible, particularly around axial slice s=50.

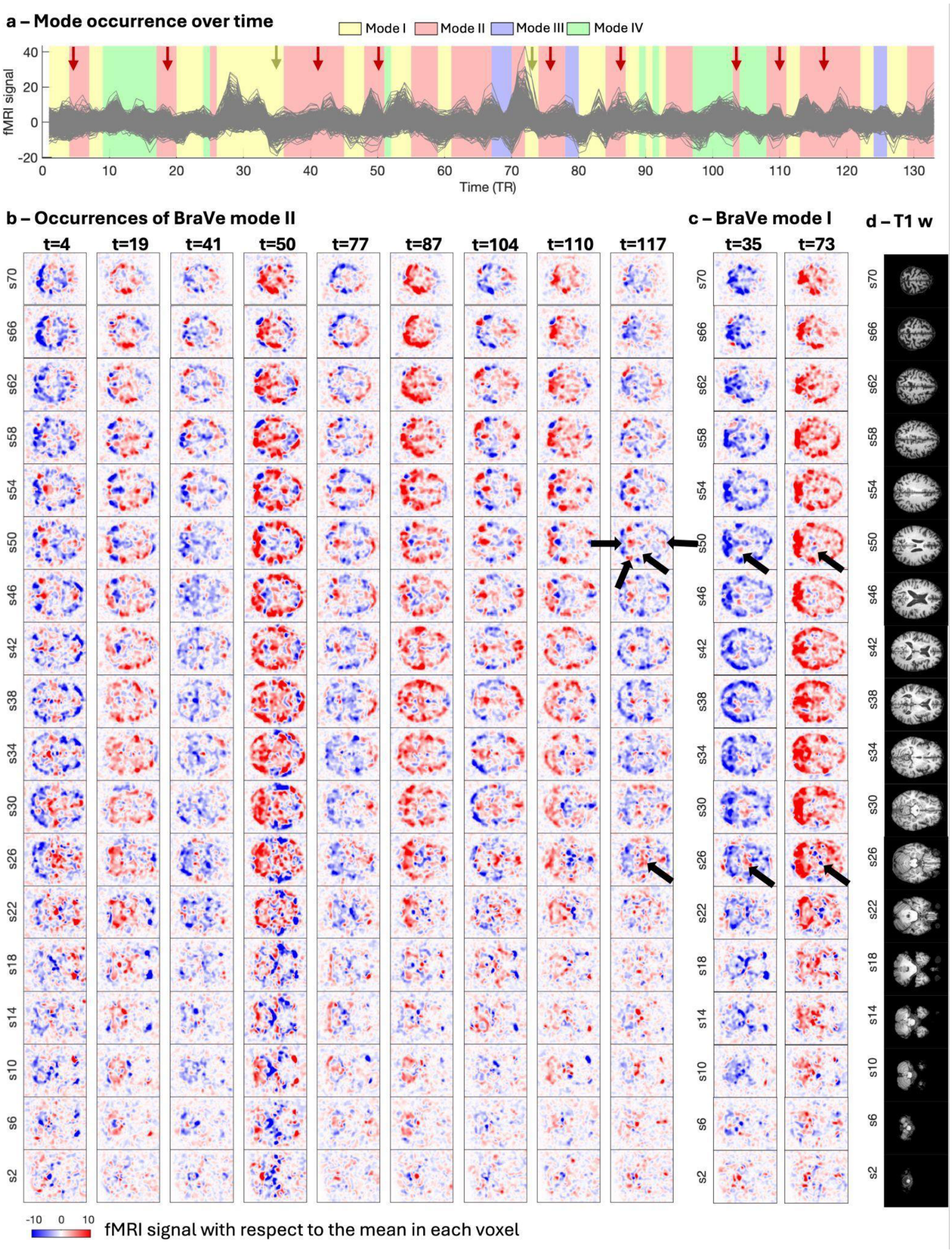
a – Mode occurrence over time
Mode I
Mode II
Mode III
Mode IV
fMRI signal
40
20
0
-20
0
10
20
30
40
50
60
70
80
90
100
110
120
130
Time (TR)
b – Occurrences of BraVe mode II
t=4
t=19
t=41
t=50
t=77
t=87
t=104
t=110
t=117
c – BraVe mode I
t=35
t=73
d – T1 w
s70
s66
s62
s58
s54
s50
s46
s42
s38
s34
s30
s26
s22
s18
s14
s10
s6
s2
-10
0
10
fMRI signal with respect to the mean in each voxel

Figure 5 - Occurrence of phase coupling modes over time. a. The fMRI signals recorded in 135 instants of time, with a TR of 3 seconds, are plotted for the entire scan duration from a CN participant (signals realigned to MNI template and with mean removed). The colored shades indicate the mode of phase coupling dominating in each instant of time. **b.** Snapshots of fMRI volumes (showing equidistant axial slices, s, from the top to the bottom of the brain) obtained in time points assigned to BraVe Mode II (corresponding to the red arrow locations in panel a). **c.** Snapshots of time points assigned to BraVe Mode I. **d**. T1-weighted MPRAGE from the same subject realigned to MNI space showing the same axial slices shown in panels b. and c.

In **Figure 5c**, we show the fMRI signals during two occurrences of BraVe mode I, one at t = 35 when the brain signals are globally above the mean (red) and another at t = 73 when the brain signals are globally below the mean (blue). Although the ventricles are not clearly visible, a close inspection to slices sl=26 to sl=50 shows fMRI signals with opposite sign in voxels overlapping with ventricle locations, as shown in the anatomical scan from the same subject shown in **panel d**.

Given that the k-means clustering employs a winner-take-all approach, each time point is assigned to a single cluster. However, this does not exclude the possibility that multiple coupling modes co-occur in the brain simultaneously, explaining the complexity of patterns observed at the instantaneous level (*e.g.* in **Figure 5b**, at time t=50, Mode II is visible in slice 50 while a different mode of coupling is visible in slice 30).

2.5. Comparisons with scores

We examined how the occupancy of the 4 functional coupling modes detected with K=4 correlate with four distinct ADNI composite cognitive scores (see Methods) as well as age and years of scholar education. The Pearson's correlation coefficients (r) and their associated p-values are reported in **Table 1**.

While the occupancy of BraVe mode I did not show any relations surviving corrections for multiple comparisons, the occupancy of BraVe Mode II, which significantly overlaps with the DMN at the cortical level, was found to correlate positively with all four cognitive scores for Memory, Executive Function, Language and Visuospatial abilities, while negatively correlating with Age. Conversely, BraVe modes III and IV did not show any relation with Age but correlated negatively with Memory and Executive function. BraVe mode IV also correlated negatively with Language scores.

	BraVe Mode I Occupancy		BraVe Mode II Occupancy		BraVe Mode III Occupancy		BraVe Mode IV Occupancy	
	r	p-value	r	p-value	r	p-value	r	p-value
Memory s=447	0.097	* 0.040	**0.16**	*** **0.00051**	**-0.16**	*** **0.00089**	**-0.18**	*** **0.00015**
Executive Function s=443	0.096	* 0.044	**0.13**	** **0.0072**	**-0.13**	** **0.0076**	**-0.17**	*** **0.00036**
Language s=465	0.060	0.20	**0.13**	** **0.0039**	-0.10	* 0.028	**-0.14**	** **0.0032**
Visuo-Spatial s=273	0.048	0.43	**0.21**	*** **0.00043**	-0.13	* 0.026	-0.14	* 0.019
Age s=599	0.10	* 0.013	**-0.14**	*** **0.00055**	0.0077	0.85	-0.071	0.081
Education s=599	0.074	0.071	-0.0025	0.95	-0.089	* 0.030	-0.043	0.30

Table 1. Occupancy of Brain-Ventricle (BraVe) coupling modes relates with cognitive scores and age. The number of scans depends on the availability of scores on the ADNI database. Asterisks indicate the level of statistical significance, with * for $p<0.05$, ** for $p<0.05/4$, *** for $p<0.05/4/6$ (surviving Bonferroni correction).

Other binary metrics, such as Marital Status, Retirement Status, Hearing Impairment and Sex, were compared using non-parametric permutation-based tests (**Table 2**). We found a strong relationship between all 4 BraVe mode occupancies and Sex. BraVe mode I was found to occur slightly more often in married participants, although not sufficiently strong to survive Bonferroni correction.

		BraVe Mode I		**BraVe Mode II**		**BraVe Mode III**		**BraVe Mode IV**	
		Mean± SEM	p-value	Mean± SEM	p-value	Mean± SEM	p-value	Mean± SEM	p-value
Marital Status	M	0.578 ± 0.09	* **0.0086**	0.135 ± 0.004	0.031	0.156 ± 0.005	0.076	0.131± 0.004	0.15
	NM	0.535 ± 0.015		0.148 ± 0.008		0.176 ± 0.010		0.140± 0.008	
Retirement Status	W	0.561 ± 0.019	0.34	0.148 ± 0.011	0.49	0.161 ± 0.011	0.14	0.130 ± 0.009	0.38
	NW	0.569 ± 0.008		0.136 ± 0.004		0.161 ± 0.005		0.134 ± 0.004	
Hearing Impairment	H	0.564 ± 0.008	0.078	0.139 ± 0.004	0.22	0.163 ± 0.005	0.16	0.134 ± 0.004	0.18
	HI	0.595 ± 0.019		0.12 8 ± 0.010		0.153 ± 0.011		0.124 ± 0.008	
Sex	M	0.618 ± 0.010	** **0.00000016**	0.129 ± 0.005	** **0.00000014**	0.137 ± 0.006	* **0.0095**	0.116 ± 0.005	** **0.00000013**
	F	0.516 ± 0.011		0.147 ± 0.006		0.186 ± 0.007		0.151 ± 0.006	

Table 2. Mean occupancy and standard error of the mean (SEM), and associated p-values from 10000 permutations of each binary metric: marital status (M= married, NM = unmarried), retirement status (W= working, NW = not working), hearing impairment (H = normal hearing; HI = hearing impaired) and sex (M= male, F = Female), across the four coupling modes. Asterisks indicate the level of statistical significance, with * for p<0.05, and ** for p<0.05/4/4.

Extending the analysis beyond the selected partition´(K=4) to the entire sample of 209 modes extracted with clustering, reveals relationships surviving the most stringent correction for multiple testing, setting a significance threshold of p=0.05/209/10=0.000024, given that 10 scores were compared for 209 modes (blue line in **Figure 6**). This extended yet stringent analysis revealed that the Memory Composite score correlates positively (r=0.21, p= 0.0000089) with the occurrence of the coupling mode obtained for K=19, c=8, corresponding to BraVe Mode V, and which overlaps at the cortical level, with the latero-Frontoparietal network, also referred to in the literature as Executive Control Network (**Figure 6** bottom left). Another mode obtained for K=11, c=11 (corresponding to BraVe Mode IV, shown in **Figure 6** bottom middle left) is the one that most strongly correlates (negatively) with the Executive Function composite score (r=-0.199, p=0.000024).

Our results also reveal an asymmetric coupling mode, detected consistently for K≥12, that occurs more often in participants with low Visuospatial abilities (r=-0.299, p=0.00000047 for K=13, c=13, shown in **Figure 6** bottom middle right and **Supplementary Figure S11**), also correlating negatively - although less significantly - with Language, Executive Function, Memory and Years of scholar Education.

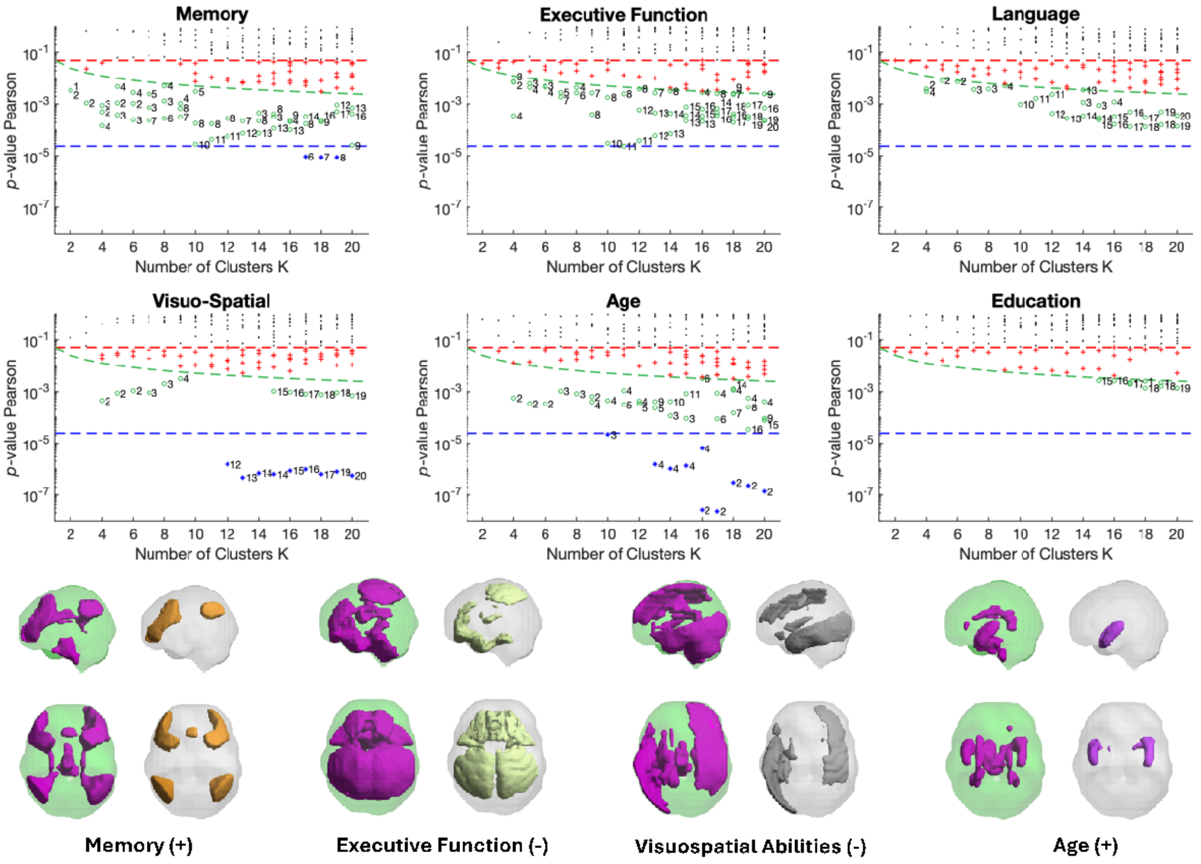

Figure 6. Statistical comparisons between mode occupancy and continuous variables. Pearson's correlation was computed between the occupancy of each mode obtained for the entire range of K explored and the four ADNI composite cognitive scores as well as age and years of scholar education. **top panel:** p-values are reported for the 6 different variables considered where colors indicate the level of statistical significance, with red representing $p_{perm} < 0.05$, green $p_{perm} < 0.05/K$ and blue representing the most stringent FWER correction with $p_{perm} < 0.00004$ accounting for all the comparisons made with the 6 continuous scores. **bottom panel:** the cluster centroids (or modes) obtained for K=19, c=8; K=11, c=11; K=13, c=13; K=17, c=2, showing for each mode (left) a magenta patch representing all the voxels dephasing with respect to the main orientation of fMRI signals and (right) a patch containing only the cortical voxels and colored according to the RSN to which they overlap the most (or grey if no overlap is found).

Finally, a BraVe mode where the left and right Insula align in phase with the signals in the ventricles was found to correlate positively with age, detected consistently for K=10, 13-20, being most significant for K=17, c=2 (r=0.226, p-value=0.0000000232, mode shown in detail in **Supplementary Figure S12**).

3. Discussion

This study provides novel insights into brain coupling dynamics by analyzing fMRI signals without distinguishing between ventricular and cortical sources. Our approach reveals new perspectives on neural connectivity and offers a unique lens through which to examine brain function. For the first time, we present an analysis that bridges the gap between resting state dynamics and brain clearance mechanisms, converging two distinct fields in neuroimaging research. While our findings are based on an existing open-source database with inherent limitations, we observed highly significant alterations across stages of cognitive decline that lays the ground for a more comprehensive understanding of brain dynamics encompassing both neural and non-neural components of brain physiology. . Importantly, the precise nature of the signals, the mechanisms organizing them across space, and their specific role in brain function remain to be fully elucidated. Our innovative analysis approach identified five main modes of Brain-Ventricle (BraVe) coupling that change significantly with cognitive decline. Three of these phase coupling modes decrease from CN to AD (BraVe mode I in earlier stages, and BraVe modes II and V in the final transition to dementia), while two others (modes III and IV) increase progressively from CN to AD.

Notably, BraVe mode I exhibits phase synchronization across the entire brain, consistent with previous findings that the prevalence of the global mode relates to better cognitive performance [14] Considering the ventricular voxels in the analysis, our results corroborate recent findings from Han et al. [5], who explored specifically the coupling between the global brain signal and CSF fluid inflow in the 4rth ventricle. In their study, the authors used a subset of the ADNI-2 dataset, focusing on subjects who had both rsfMRI and PET measurements, as well as Mini-Mental State Examination (MMSE) scores. Our results, using a larger sample size (due to less stringent inclusion criteria) and a distinct analysis framework unspecific to anatomical location corroborate their main finding with greater statistical significance.

While the first BraVe coupling mode has already been subject of studies, we identified additional modes of coupling between the brain and ventricles with more complex spatial configurations, some of which revealing known RSNs. To our knowledge, the relationship between brain-ventricle coupling at rest and RSNs has not yet been fully clarified. Despite the accumulating evidence demonstrating that RSNs are involved with healthy and pathological brain function, the physiological nature of ‘intrinsic connectivity networks (ICNs)’, ‘resting-state networks (RSNs)’ or ‘functional gradients’ has not been fully disambiguated [8,44]. While there have been attempts to propose that RSNs are associated with physiological components of the brain, the field of fMRI research generally assumes that the signals captured with Echo-Planar Imaging (EPI) in the gray matter areas, once adequately preprocessed to remove physiological components, are directly associated with neurovascular coupling. Here, we do not directly exclude this hypothesis, but avoid using the term BOLD to refer to EPI signals from gray matter, because we believe further studies are needed to determine whether resting-state signal fluctuations are strictly BOLD-related or have a more direct relationship with the fMRI signals in the ventricles, potentially linked with either CSF inflow/outflow into the brain or subtle spatial displacements induced by pulsatile motion.

Using the current dataset, we cannot definitively determine the origin of the signal fluctuations. What we know is that at specific moments during the scan, the time of spin-spin dephasing following a radiofrequency pulse, T2*, captured with Echo Planar Imaging (EPI) in the MR scanner, increases in certain brain voxels while decreasing in others, forming spatially organized patterns of phase alignment. We also find that there is a repertoire of preferred modes of phase alignment, and the proportion of time spent in some of these modes relates with cognitive preservation, so it is crucial to gain a better understanding of their origin, role and organizing principles.

The T2*-weighted EPI MRI signal is sensitive to changes in magnetic field homogeneity, with temporal increases indicating moments when the local magnetic environment becomes more homogeneous and therefore the spins take longer to diphase, when compared to the average T2* of that same voxel over the entire recording time, $\Delta T2^*$ (**Figure 7**). These changes may result from variations in blood oxygenation, CSF flow, or subtle spatial displacements at tissue-fluid interfaces affecting local magnetic susceptibility. While identifying the specific mechanism exceeds our current scope, our finding that these magnetic field homogeneity changes are spatially organized across the entire brain, synchronizing between ventricles and established RSNs, challenges current assumptions about resting-state signal fluctuations.

The conventional explanation is that resting-state fluctuations are driven by neuronal firing, which is known to trigger a hemodynamic response increasing blood oxygenation through neurovascular coupling[44]. However, this neurovascular coupling inadequately accounts for spatially coordinated signal fluctuations detected in spontaneous activity, beyond the fact that high neuronal firing sufficient to trigger an inflow of oxygenated blood at this macroscopic scale may not be plausible in the resting state from an energy efficiency perspective. Additionally, motion from cardiac and respiratory activity occurs at faster frequencies (~1Hz and ~0.3Hz respectively) than those characterizing resting-state fluctuations in brain signals (<0.1Hz). While the dataset used in this study employs a TR of 3 seconds, limiting the precise detection of resonant frequencies associated with oscillatory processes, previous work in rodents using high temporal resolution fMRI detected clear oscillatory modes at macroscopic scales and ultra-slow frequencies (Cabral et al., 2023). These spatial coupling patterns are consistent with the eigenmode resonance phenomena described by Pang et al. (2023, Nature), who proposed that these patterns are shaped by brain geometry. The brain's structural architecture may create natural resonance patterns that manifest as the T2*-weighted signal variations observed here. However, despite these advances, the precise nature and medium from which these phenomena generate remains unclear and requires further investigation, particularly with higher temporal resolution to verify the resonance quality of these modes.

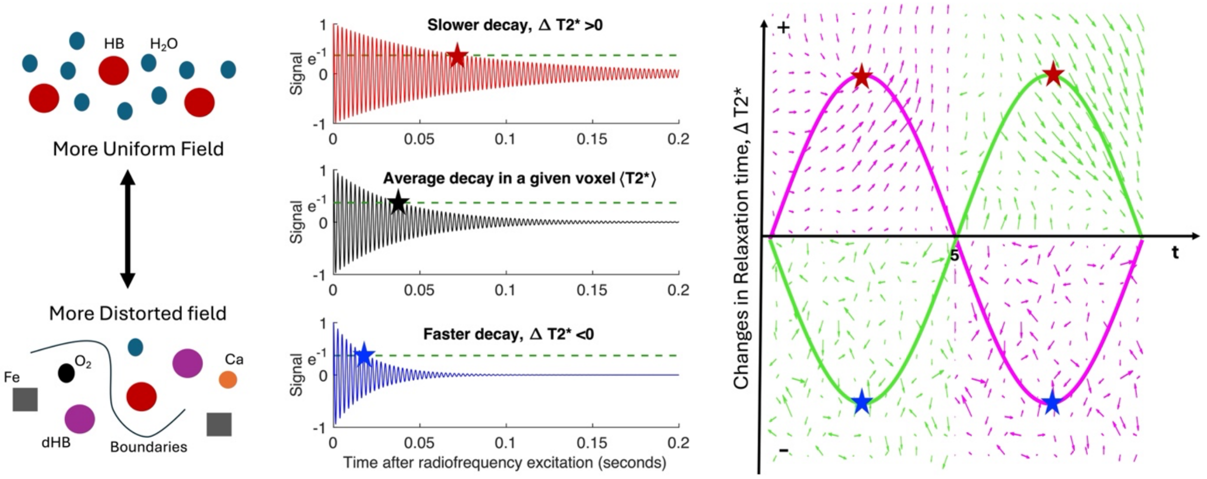

Figure 7 – General interpretation of fMRI signal fluctuations. (Left) The signals captured with Echo-Planar Imaging are sensitive to magnetic field inhomogeneities within each voxel, which impact the T2* relaxation time. Higher inhomogeneities cause protons to precess at slightly different frequencies, leading to a faster loss of coherence and signal decay. (Middle) Positive signal values (relative to the mean) indicate increased local magnetic field homogeneity, resulting in longer T2* relaxation times. Conversely, negative values reflect greater field heterogeneity, causing faster signal decay and shorter T2* times. (Right) The fact that field homogeneity alternates over time between longer and shorter T2*, and increases in some spatial locations while decreasing in others, suggests the existence of a resonant process in brain activity.

An alternative hypothesis suggests that this ultra-slow activity relates to glymphatic pulsation mechanisms[7], with neuronal activity maintaining lower firing levels—more plausible during rest. This offers a different explanation for long-range correlations in spontaneous activity which, rather than reflecting axonal connections between distant brain areas, may indicate distinct anatomical locations equally affected by these pulsations. This potentially explains the symmetric alignment of RSNs, with poles consistently found over gyri and brain fissures. These possibilities open new perspectives on brain physiological processes supporting both network function and neuroprotection, which appear crucial for cognitive preservation.

3.1 Transitions between cognitive stages

The gradual cognitive deterioration across the four cognitive stages is associated with distinct modes of Brain-Ventricle coupling. Notably, the transition from CN to EMCI is characterized by a decrease in BraVe Mode I and increased occurrence of BraVe Mode III. Previous research has already attempted to explore the transition from CN individuals to EMCI from the perspective of RSNs. For instance, McKenna et al. [45] used a subset of the ADNI dataset and incorporated the presence of the Apolipoprotein E allele e4 (APOE e4) as a covariate. Consistent with our findings, their study revealed disrupted connectivity in EMCI, particularly in key regions such as the cingulate cortex and its connections with anterior and posterior MPFC. Moreover, they observed that this functional connectivity disruption is strongly linked to levels of the APOE e4 protein in CSF samples [45]. Although there are differences in the methodologies between our study and theirs, it is plausible that the results we have obtained could be associated with this genetic factor. However, a comprehensive understanding of the role of genetics in the observed functional coupling alterations requires further investigation.

Since we detected significant alterations in functional coupling already at the EMCI stage, we cannot exclude the possibility that these changes may occur even before the biochemical alterations become evident. It remains unclear whether the biochemical alterations precede the disruptions in brain-ventricle coupling, or if the latter occur at earlier stages. Further research is needed to clarify the sequence of these events and whether the observed functional connectivity changes might serve as an early indicator of cognitive decline, possibly even before the biochemical markers are detectable.

Previous research has explored functional brain connectivity changes across neurodegeneration stages, but with limitations. For instance, one study used only a small portion of the ADNI2 database, which weakened its statistical power [46]. That study detected significant default mode network (DMN) differences only in early mild cognitive impairment (EMCI) patients. Our research, however, identified DMN alterations when comparing Alzheimer's disease (AD) patients not only with cognitively normal (CN) individuals but also with both EMCI and late mild cognitive impairment (LMCI) groups.

Interestingly, regions within the DMN are among the first areas where Aβ deposition begins, occurring years before a formal AD diagnosis[47]. In particular, it was seen that global glymphatic function—measured by the coupling between global brain activity and the CSF flow—has a strong association with various Aβ and tau markers at the early stages of AD pathology, indicating that resting-state brain activity may influence Aβ accumulation in the initial stages of the pathology, possibly through its effect on glymphatic clearance. The spatial differentiation into more complex modes of Brain-Ventricle coupling further highlights how certain brain regions may be more vulnerable due to impaired glymphatic function, with potential impact in the understanding of other neurological or psychiatric conditions beyond cognitive decline.

Other abnormal functional connectivity changes have also been reported in AD. For instance, previous studies have suggested disrupted functional integration within the cerebellum, DMN, FPN, visual network, and sensorimotor network in AD patients compared to controls [48].

Additionally, functional connectivity in the Frontoparietal network has been found to be significantly reduced in AD compared to controls [25], aligning with our findings. Notably, some studies consider the FPN as a synonym for the Central Executive Network (CEN), while other studies consider the CEN as a part of the FPN but yet a different network. To date, there is no consensus on a unified network taxonomy: some nomenclatures are based on anatomical terminology (*e.g.*, “frontoparietal”, “occipital”), while others refer to network functionality (*e.g.*, “central executive”, “salience”)[49].

In our study, notably, as the number of clusters increases, the “classical” RSNs begin to split into distinct components (e.g., the DMN in K = 17, C = 4, and K = 17, C = 11; see **Figure 4**). Uddin et al.[49] found that, with fine ICA parcellations and an increasing number of clusters, the DMN begins to divide into subsystems: frontal, ventral prefrontal, anterior and medial temporal lobe regions, which further split into additional components as the clustering increases. These findings provide insights into the complexity of the brain's hierarchical organization, which remains an area of speculation. Different methodologies yield varying results, definitions, parcellations, and nomenclatures, contributing to the challenge of consistently replicating the exact results across studies.

All the phase coupling modes we identified included the ventricles, which exhibited a shift in phase from the rest of the brain. We cannot determine whether it is neuronal activity that alters ventricular activity or, conversely, if the activity in the ventricles is affecting neuronal activity. Given that the CSF also propagates through the brain parenchyma, our findings do not exclude the possibility that the ultraslow signals detected in gray matter with fMRI share the same biophysical origin as the signals observed in the ventricles.

Regardless of the direction of influence, the differences we found in the coupling modes are clear and exhibit strong statistical power. Therefore, it is crucial for future research to investigate the origin of this altered signal, as it may contribute to the altered functional connectivity patterns observed in dementia, which may not necessarily originate from neuronal processes.

One important implication of this study is that it challenges the standard preprocessing applied to fMRI data to remove CSF components, and could open up the possibility to re-analyse existing fMRI datasets. This type of analysis can be applied to virtually all previously recorded ‘whole-brain’ fMRI scans, but from which the physiological signals have been removed as sources of noise. This allows revisiting old data using a novel analysis framework that could potentially reveal important insights into different neurological disorders and psychiatric syndromes [50–52].

3.2 Limitations

One limitation of the study is the relatively poor temporal resolution (TR= 3 seconds) of the fMRI scans used in this study, which limits the analysis of phase dynamics in the temporal domain. While recent studies with faster temporal resolution point to the existence of oscillatory/pulsatile processes occurring at ultra-slow frequencies in the brain[2,7,9,53,54] a full understanding of the phase relationships observed in this study would require higher temporal resolution. Still, although the current EPI fMRI sequences lack the specificity and temporal resolution to directly understand the origin of the signals, the fact that we identified alternations between positive and negative activations in brain-ventricle coupling dynamic suggests that CSF flow in the ventricles may play a critical role in maintaining these oscillatory mechanisms. Moreover, while recent studies have proposed that RSNs represent resonant modes shaped by brain geometry [55]our findings open up new avenues for investigating how CSF flow in the ventricles contributes to the broader ultra-slow oscillatory dynamics of the brain.

Another limitation of the study is the fact that we overlooked the impact of brain atrophy that occurs naturally with aging, with many morphological and volumetric changes being documented both in cognitively normal as in cognitively impaired patients (cfr. [56] for a review). Although the MNI template is widely used in studies involving elderly populations, being obtained from the brains of young adults may lead to discrepancies in aligning and interpreting brain structures during spatial normalization. Nevertheless, the current analysis framework focused on macroscopic modes of phase alignment rather than precise anatomical locations, combined with a large sample size and conservative statistics reinforce the validity of our results.

In our sample, the CN are slightly older than the AD patients, which is noteworthy because cognitive decline typically increases with age. If the AD group had been older than the CN group, we could have attributed the differences in RSNs to age-related decline. However, despite being younger, the AD patients in our study astill exhibit impaired RSN function, which did not correlate with age, indicating that the observed network impairments are more likely related to the pathological progression of AD rather than to aging.

More importantly, it is now recognized that the clinical and biological presentations of AD do not always coincide. For instance, pathological changes can occur without any clinical manifestation of dementia or MCI[57,58]. For this reason, the International Working Group for New Research Criteria for the Diagnosis of AD, in 2007, proposed new diagnostic criteria, allowing for a diagnosis of AD based on both biological and clinical evidence[59,60]. However, the ADNI 2 inclusion criteria consider only clinical evidence, without accounting for biological markers (for a detailed overview, refer to the ADNI2 procedure manual) and beta-amyloid and tau levels, despite being available only for a limited number of scans sacrificing statistical power, often preceded the rs-fMRI scans by many years, making direct comparisons unreliable Therefore, including biological classifications for CN/MCI/AD obtained at the time of scanning in future studies may provide better insights into the relation of these biological markers with the occupancy brain-ventricle coupling modes, and whether the latter even precedes biological markers

5. Methods

5.1. Study population

The study included 163 unique subjects (32 AD patients, 53 EMCI, 40 LMCI and 38 healthy controls, referred to as “cognitively normal”, CN) from the North American multicenter Alzheimer's Disease Neuroimaging Initiative (ADNI; https://adni.loni.usc.edu). ADNI inclusion and exclusion criteria are detailed at http://www.adni-info.org procedures manual. For our study, we included all the N=163 subjects from the ADNI2 phase who had both structural and resting-state functional magnetic resonance imaging (rsfMRI) scans.

We extracted from the ADNI database the sex, age and years of scholar education, as well as marital status, retirement status and presence of hearing impairment. Specifically, information on marital and employment status was extracted from the ADNI Subject Demographics table (specifically, the PTMARRY, PTNOTRT and PTWORK columns). The values for hearing impairment were obtained by comparing reports in the Neurological Exam, Physical Exam, and Recent Medical History Details Log tables, as done by Llano et al.[61].

Demographics of the subjects can be found on **Table 3**.

ADNI (N= 163)	CN (A)	EMCI (B)	LMCI (C)	AD (D)	*p*-values
Sex	17 M, 21 F	21 M, 32 F	24 M, 16 F	15 M, 17 F	A - B = 0.6; A - C = 0.2; A - D = 1; B - C = 0.06; B - D = 0.6; C - D = 0.3
Mean age (SD)	75.5 (7.05)	71.3 (6.55)	72 (8.16)	72.6 (7.2)	**A - B = 0.004**; **A - C = 0.04**; A - D = 0.9; B - C = 0.6; B - D = 0.4; C - D = 0.7
Mean years of education (SD)	16.39 (2.17)	15.6 (2.6)	16.8 (2.43)	15.49 (2.7)	**A - B = 0.002**; A - C = 0.1; **A - D = 0.03**; **B - C = 2e-05**; B - D = 0.7; **C - D = 7e-05**
Marital status	29 MA, 3 DI, 3 W, 3 NM	37 MA, 10 DI, 3 W, 3 NM	30 MA, 1 DI, 8 W, 1 NM	28 MA, 2 DI, 2 W, 0 NM	A - B = 0.5; A - C = 0.2; A - D = 0.4; **B - C = 0.02**; B - D = 0.2; C - D = 0.3
Retirement status	32 R; 6 NR	42 R; 11 NR	34 R; 6 NR	29 R, 3 NR	A - B = 0.6; A - C = 1; A - D = 0.5; B - C = 0.6; B - D = 0.2; C - D = 0.7
Hearing impairment	30 NH, 8 HI	49 NH, 4 HI	36 NH, 4 HI	24 NH, 8 HI	A - B = 0.1; A - C = 0.2; A - D = 0.8; B - C = 0.7; **B - D = 0.05**; C - D = 0.1

Table 3. Baseline characteristics of 163 unique subjects from ADNI used in this study. p-values are derived from 2-sample t-tests for continuous measures, and Fisher's exact test for categorical measures. Statistically significant differences ($p < 0.05$) in each comparison were marked using a bold font. AD = Alzheimer disease participants; ADNI = Alzheimer's Disease Neuroimaging Initiative; CN = cognitively normal; DI = divorced; EMCI, early mild cognitive impairment; HI = hearing impairment; LMCI = late mild cognitive impairment; M/F = male/female; MA = married; NH = normal hearing; NM = non married; NR = not retired from work; R = retired from work; SD = standard deviation; W = widowed.

Each subject had an fMRI scan and behavioral data collected at the baseline visit, and then most of them had follow-up scans and behavioral measurements at 3 months, 6 months, 1 year and 2 years after the baseline visit, resulting in a total of S=599 scans (157 scans from CN controls, 189 from ECMI, 147 from LMCI and 106 from AD patients).

5.2. Phenotypic Harmonization Consortium cognitive scores

To examine relations between mode occupancy and cognitive performance, we used the ADNI cognitive composite scores, which integrate multiple neuropsychological tests including the Mini Mental State Examination (MMSE), Montreal Cognitive Assessment (MoCA), and

Alzheimer's Disease Assessment Scale – Cognitive Subscale (ADAS-Cog) into four cognitive domains:

- *Memory (ADNI-Mem)*: This composite score incorporates the Rey Auditory Verbal Learning Test (RAVLT), ADAS-Cog Word Recall, Delayed Word Recall, Orientation, and Word Recognition, Logical Memory (immediate and delayed) from the Wechsler Memory Scale-Revised (WMS-R), relevant MMSE items (immediate recall, delayed recall, orientation), and MoCA delayed recall and registration scores [62].
- *Executive Function (ADNI-EF)*: This composite includes the Clock Drawing Test (CDT) command scores, Trail Making Test (TMT), Wechsler Adult Intelligence Scale-Revised (WAIS-R) Digit Span (Forward and Backward) and Digit Symbol tasks, ADAS-Cog number cancellation, MMSE backward spelling, and relevant MoCA executive function items [63].
- *Visuospatial Function (ADNI-VS)*: This composite incorporates CDT copy tasks, ADAS-Cog Constructional Praxis, and MMSE drawing tasks [63].
- *Language (ADNI-Lan)*: This composite includes Category Fluency (Animals/Vegetables), Boston Naming Test (BNT), and language-related items from the MoCA, MMSE, and ADAS-Cog [63].

These composites were psychometrically optimized to maximize measurement precision while minimizing floor and ceiling effects. Higher scores indicate better cognitive performance across all domains. These 4 composite scores were obtained at most but not all fMRI sessions, resulting in S=447 fMRI scans with associated Memory score, S=443 scans with Executive Function score, S=465 scans with Language score and S=273 scans with Visuospatial score.

5.3. MRI acquisition parameters

All MRI data from the ADNI study were acquired using 3 Tesla MR scanners at various participating sites, following the standardized ADNI2 protocol. The scanners used were from recent models produced by General Electric (GE, Chicago, United States), Philips Medical Systems (Philips, Amsterdam, Netherlands), and Siemens Medical Solutions (Siemens, Erlangen, Germany) (full acquisition details can be found at http://adni.loni.usc.edu/methods/documents/mri-protocols/).

rsfMRI volumes were collected with an echo-planar image (EPI) sequence (flip angle = 80°, spatial resolution = 3 × 3 × 3 mm3, slice thickness = 3.3 mm; with TR/TE (repetition time / echo time) = 3000/30 ms. Each fMRI scan lasted 7 minutes. In addition, an MPRAGE sequence TR/TE = 2300/3.1 ms was used for anatomical segmentation and template normalization.

5.4. fMRI preprocessing

The rsfMRI data preprocessing was conducted using CONN's default minimal preprocessing pipeline (https://web.conn-toolbox.org, release 21.a) for volume-based analyses with direct normalization to MNI-space[64,65]. This pipeline encompasses four main steps:

1. Functional realignment and unwarping: Using SPM12's realign & unwarp procedure [66], all volumes were co-registered to the first (reference) volume using b-spline interpolation. This step also compensates for susceptibility distortion-by-motion interactions by computing deformation field derivatives relative to head movement.
2. Slice-timing correction: The functional data underwent temporal alignment using SPM12 with sinc-interpolation.

3. Spatial normalization: Both functional (rsfMRI) and structural (T1-weighted MPRAGE) images were normalized to MNI space using SPM12's unified segmentation and normalization algorithm [67]. This direct normalization process used a 180x216x180mm bounding box, with 2mm and 1mm isotropic voxels for functional and anatomical data respectively, implemented with 4th order spline interpolation.
4. Spatial smoothing: The final step applied an 8mm FWHM Gaussian kernel to the functional data to minimize inter-subject variability in functional and gyral anatomy.

All subsequent analyses were performed on MATLAB version R2024B (see Code Availability statement). The first 5 volumes in each rsfMRI scan were discarded to eliminate nonsteady-state effects that occur while the signal reaches equilibrium at the start of each functional run. The voxel time-series were then bandpass filtered between 0.01-0.1 Hz to isolate the low-frequency fluctuations which have been shown to correlate over long distances, while removing components from cardiac and respiratory cycles (>0.1 Hz) and scanner drift (<0.01 Hz) [68,69].

5.5. fMRI data analysis

Given the particular goal of this study to analyze fMRI signals from the brain, irrespective of their anatomical location, instead of averaging the fMRI signals into Regions-of-Interest (ROI) defined from a parcellation template, we opted instead to perform the analysis considering each cubic voxel inside the MNI brain mask as a ROI. We considered the MNI template with 1 cubic centimeter voxels, which contains N=1821 voxels covering the entire brain. The fMRI volumes from each subject - already aligned in MNI space - were then downsampled from 2mm^3 to 10mm^3 using linear interpolation, and the N=1821 voxels inside the MNI brain mask were treated as brain parcels. This downsampling is acceptable given that i) the signals were spatially smoothed with a gaussian kernel of 8mm in preprocessing steps and ii) the high variability between subjects is reduced with larger voxels.

To investigate the existence of recurrent phase-coupling modes, and whether their occurrence varied with AD progression, we applied the Leading Eigenvector Dynamics Analysis (LEiDA) methodology [14]. Following the LEiDA algorithm, the Hilbert transform was applied to the 1xT time series in each of the N=1821 voxel time series to extract the fMRI signal phase θ in each voxel. For each time instant (between t=2 and t=T-1), we compute the $1xN$ leading eigenvector of the N×N matrix of phase coherence (obtained using $cos(\theta(n, t) - \theta(p, t)$, with n and p corresponding to pairs of voxels). A total of 81707 'instantaneous' leading eigenvectors was obtained from all the 599 scans, each representing how the fMRI signals in all the N voxels are organized in terms of phase relationship at each instant of time.

These leading eigenvectors, which capture the phase alignment of fMRI signals observed across scans at all time points, were then categorized into K clusters through k-means clustering, using the cosine distance to evaluate the cluster-to-centroid distance. Given the unpredictability of the precise number of functional coupling modes, K was varied from 2 to 20, and the results were analyzed across the explored partition range, ensuring result stability with 500 replicates[14,70].

The clustering assigns a single cluster/mode to each time point by selecting the closest centroid at each time point. Using these cluster time courses, we calculated the Occupancy of each mode in each scan, which is the number of time points assigned to a given state divided by the total number of time points (TRs) in each scan. The occupancies of each mode obtained with k ranging from 2 to 20 were calculated for each scan [14].

5.6. Statistical analyses

To detect coupling modes whose occupancy differs significantly between groups, we first assessed the equality of variances in the distributions of occupancy values using Levene's test. When the assumption of equal variances was met, we applied a permutation-based paired t-test. When Levene's test indicated unequal variances, we instead used Welch's t-test to account for this heteroscedasticity[51]. This non-parametric approach uses permutations of group labels to estimate the null distribution, which is computed independently for each experimental condition. For each of the 100,000 permutations, the appropriate t-test (standard or Welch's) was conducted to compare populations, resulting in a p-value for each comparison.

We evaluated the statistical significance of our results considering the FWER by plotting the p-values against various significance thresholds. Specifically, we used the standard threshold of $\alpha_1 = 0.05$ (shown in red), the Bonferroni corrected threshold $\alpha_2 = 0.05/K$ (shown in green) to correct for the number of independent hypotheses tested in each partition model (with α_2 decreasing as K increases), and $\alpha_3 = 0.05/\sum(K=2:K=25)=0,00015$ (shown in blue), which conservatively adjusts for all comparisons, whether dependent or independent[71].

Given that multiple modes were compared, which increases the chances of false positives, we consider only the modes whose difference between groups survives correction for multiple comparisons.

To detect functional states whose probability of occurrence correlates with continuous scores such as composite scores for memory, executive function, language, visuospatial abilities, years of education and age, we computed Pearson's correlation between the probability of occurrence in every scan with the corresponding score[72,73].

To compare with binary scores such as indicators of social isolation and sex, we performed the same permutation test described above, also testing for equality of variances and with 100,000 permutations.

5.7 Visualization of cluster centroids

The cluster centroids are *1xN* vectors, where each of the *N=1821* elements corresponds to a cubic centimeter voxel in the brain. The cluster centroids obtained in $10mm^3$ were resized to $2mm^3$ using a linear interpolation for better visualization. Using concepts from analytic geometry, the values in each vector element refer to the projection (*i.e.*, cosine of the phase) of each voxel into the leading eigenvector, which defines the main orientation of all signal phases. The sign of the vector elements depends on whether the phase difference (to the leading eigenvector) is smaller or larger than 90°. As such, grouping all the voxels according to their sign in the cluster centroid, reveals two communities, where the smallest community reveals the brain areas varying in anti-phase with the rest of the brain.

5.8 Overlap with RSNs

The overlap with seven reference resting state networks (RSNs)[43] was then calculated for each of the cluster centroids obtained. Given that the template of 7 RSNs is available in $2mm^3$ MNI space, the cluster centroids obtained in $10mm^3$ were resized to $2mm^3$ and the overlap was calculated by computing the Pearson correlation between the binary masks of each network (considering only cortical voxels) with the corresponding binary mask of the cluster centroids (setting 1 to all the voxels with positive value in the leading eigenvector and 0 otherwise). The cluster centroids were colored with the original paper's color scheme[43].

Acknowledgements

Data collection and sharing for this project was funded by the Alzheimer's Disease Neuroimaging Initiative (ADNI) (National Institutes of Health Grant U01 AG024904) and DoD ADNI (Department of Defense award number W81XWH-12-2-0012). ADNI is funded by the National Institute on Aging, the National Institute of Biomedical Imaging and Bioengineering, and through generous contributions from the following: AbbVie, Alzheimer's Association; Alzheimer's Drug Discovery Foundation; Araclon Biotech; BioClinica, Inc.; Biogen; Bristol-Myers Squibb Company; CereSpir, Inc.; Cogstate; Eisai Inc.; Elan Pharmaceuticals, Inc.; Eli Lilly and Company; EuroImmun; F. Hoffmann-La Roche Ltd and its affiliated company Genentech, Inc.; Fujirebio; GE Healthcare; IXICO Ltd.; Janssen Alzheimer Immunotherapy Research & Development, LLC.; Johnson & Johnson Pharmaceutical Research & Development LLC.; Lumosity; Lundbeck; Merck & Co., Inc.; Meso Scale Diagnostics, LLC.; NeuroRx Research; Neurotrack Technologies; Novartis Pharmaceuticals Corporation; Pfizer Inc.; Piramal Imaging; Servier; Takeda Pharmaceutical Company; and Transition Therapeutics. The Canadian Institutes of Health Research is providing funds to support ADNI clinical sites in Canada. Private sector contributions are facilitated by the Foundation for the National Institutes of Health (www.fnih.org). The grantee organization is the Northern California Institute for Research and Education, and the study is coordinated by the Alzheimer's Therapeutic Research Institute at the University of Southern California. ADNI data are disseminated by the Laboratory for Neuro Imaging at the University of Southern California.

The Center for Music in the Brain (MIB) is funded by the Danish National Research Foundation (project number DNRF117).

FFC Ph.D. Scholarship was funded by POR Puglia FESR FSE 2014-2020, CUP: H99121006630008.

SN is supported by the Italian Ministry of Research, under the complementary actions to the NRRP "Fit4MedRob - Fit for Medical Robotics" Grant (# PNC0000007).

This publication was also produced with the co-funding European Union - Next Generation EU, in the context of The National Recovery and Resilience Plan, Investment Partenariato Esteso PE8 "Conseguenze e sfide dell'invecchiamento", Project Age-It (Ageing Well in an Ageing Society), CUP: B83C22004800006.

JC is supported by La Caixa Foundation, Spain (LCF/BQ/PR22/11920014) and the Foundation for Science and Technology, Portugal (UIDB/50026/2020, UIDP/50026/2020).

Credit Author Statement

FFC: Investigation, Formal analyses, Data curation, Writing - Original Draft, Writing - Review & Editing; **EB:** Conceptualization, Supervision, Writing - Review & Editing; **VM:** Formal analyses, Writing - Review & Editing (contribution to section 5.3); **SN:** Writing - Review & Editing; **BT:** Writing - Review & Editing; **GL:** Supervision, Writing - Review & Editing; **JC:** Conceptualization, Investigation, Supervision, Methodology, Software, Formal analyses, Data Curation, Visualization, Writing - Original Draft, Writing - Review & Editing.

Data availability statement

The data used in this study (including raw MRI data and scores) can be downloaded from the ADNI database https://adni.loni.usc.edu/ following access request.

The eigenvectors extracted from 599 minimally-preprocessed fMRI scans, as well as the cluster centroids and statistical results, are freely available for download at: https://codeocean.com/capsule/8407134/tree.

Code availability statement

The MATLAB scripts developed for the analysis and figure generation are freely available for download at: https://codeocean.com/capsule/8407134/tree

Ethics & Inclusion Statement

This research was conducted as a collaborative effort between researchers from multiple institutions across Portugal, Italy and Denmark. The study's focus on brain dynamics over distinct stages of cognitive decline represents a topic of global scientific importance with relevance to the neuroscience communities in the participating countries. Roles and responsibilities were clearly defined at project initiation, with specific expertise from each collaborator acknowledged and leveraged. The senior researchers mentored junior team members throughout the project, providing opportunities for skill development in analysis methods of neuroimaging data. All authors met the Global Code of Conduct for Equitable Research Partnerships criteria for authorship, contributing substantially to conception, data analysis, manuscript drafting, and critical revision.

This research utilized data from the Alzheimer's Disease Neuroimaging Initiative (ADNI) database (adni.loni.usc.edu). The ADNI study was conducted according to Good Clinical Practice guidelines, the Declaration of Helsinki, and U.S. 21 CFR Part 50 (Protection of Human Subjects) and Part 56 (Institutional Review Boards). Written informed consent was obtained from all participants before protocol-specific procedures were performed. The ADNI study was approved by the institutional review boards of all participating institutions. All ADNI sites had local Institutional Review Board approval for human subjects research. The present analysis was performed in accordance with the ADNI data usage agreement and did not require additional ethical approval as it involved secondary analysis of de-identified data.

All computational work adhered to open science practices, with code documentation standards maintained at the highest level across all participating institutions. The researchers followed institutional policies regarding data management and intellectual property, with agreements in place for open-access publication of the findings. Our literature review and citations deliberately include research from a diverse range of geographical regions and institutions to acknowledge the global nature of neuroscience research.

References

1. Kramarow, E. A. Diagnosed Dementia in Adults Age 65 and Older:United States, 2022. *Natl Health Stat Report* 1–9 (2024).
2. Fultz, N. E. *et al.* Coupled electrophysiological, hemodynamic, and cerebrospinal fluid oscillations in human sleep. *Science* **366**, 628–631 (2019).
3. Roefs, E. C. A., Eiling, I., de Bresser, J., van Osch, M. J. P. & Hirschler, L. BOLD-CSF dynamics assessed using real-time phase contrast CSF flow interleaved with cortical BOLD MRI. *Fluids and Barriers of the CNS* **21**, 1–10 (2024).
4. Lewis, L. D. The interconnected causes and consequences of sleep in the brain. *Science* **374**, 564–568 (2021).
5. Han, F. *et al.* Reduced coupling between cerebrospinal fluid flow and global brain activity is linked to Alzheimer disease-related pathology. *PLoS Biol.* **19**, e3001233 (2021).
6. Han, F. *et al.* Decoupling of Global Brain Activity and Cerebrospinal Fluid Flow in Parkinson's Disease Cognitive Decline. *Mov Disord* **36**, 2066–2076 (2021).
7. Kiviniemi, V. *et al.* Ultra-fast magnetic resonance encephalography of physiological brain activity - Glymphatic pulsation mechanisms? *J. Cereb. Blood Flow Metab.* **36**, 1033–1045 (2016).
8. Chen, J. E. *et al.* Resting-state 'physiological networks'. *Neuroimage* **213**, 116707 (2020).
9. Cabral, J., Fernandes, F. F. & Shemesh, N. Intrinsic macroscale oscillatory modes driving long range functional connectivity in female rat brains detected by ultrafast fMRI. *Nat. Commun.* **14**, 375 (2023).
10. Raut, R. V. *et al.* Global waves synchronize the brain's functional systems with fluctuating arousal. *Sci. Adv.* **7**, eabf2709 (2021).
11. Liu, X., Zhang, N., Chang, C. & Duyn, J. H. Co-activation patterns in resting-state fMRI signals. *Neuroimage* **180**, 485–494 (2018).
12. Lv, H. *et al.* Resting-State Functional MRI: Everything That Nonexperts Have Always Wanted to Know. *AJNR Am. J. Neuroradiol.* **39**, 1390–1399 (2018).
13. Fox, M. D. *et al.* The human brain is intrinsically organized into dynamic, anticorrelated functional networks. *Proc. Natl. Acad. Sci. U. S. A.* **102**, 9673–9678 (2005).
14. Cabral, J. *et al.* Cognitive performance in healthy older adults relates to spontaneous switching between states of functional connectivity during rest. *Sci. Rep.* **7**, 1–13 (2017).
15. Grieder, M., Wang, D. J. J., Dierks, T., Wahlund, L.-O. & Jann, K. Default Mode Network Complexity and Cognitive Decline in Mild Alzheimer's Disease. *Front. Neurosci.* **12**, 770 (2018).
16. Cha, J. *et al.* Functional alteration patterns of default mode networks: comparisons of normal aging, amnestic mild cognitive impairment and Alzheimer's disease. *Eur. J. Neurosci.* **37**, 1916–1924 (2013).
17. Ouchi, Y. & Kikuchi, M. A review of the default mode network in aging and dementia based on molecular imaging. *Rev. Neurosci.* **23**, 263–268 (2012).
18. Ibrahim, B. *et al.* Diagnostic power of resting-state fMRI for detection of network connectivity in Alzheimer's disease and mild cognitive impairment: A systematic review. *Hum. Brain Mapp.* **42**, 2941–2968 (2021).
19. Brier, M. R. *et al.* Loss of intranetwork and internetwork resting state functional connections with Alzheimer's disease progression. *J. Neurosci.* **32**, 8890–8899 (2012).
20. Gili, T. *et al.* Regional brain atrophy and functional disconnection across Alzheimer's disease evolution. *J. Neurol. Neurosurg. Psychiatry* **82**, 58–66 (2011).
21. Griffanti, L. *et al.* Effective artifact removal in resting state fMRI data improves detection of DMN functional connectivity alteration in Alzheimer's disease. *Front. Hum. Neurosci.* **9**, 449 (2015).
22. Wang, Z. *et al.* Differentially disrupted functional connectivity of the subregions of the amygdala in Alzheimer's disease. *J. Xray Sci. Technol.* **24**, 329–342 (2016).
23. He, X. *et al.* Abnormal salience network in normal aging and in amnestic mild cognitive impairment and Alzheimer's disease. *Hum. Brain Mapp.* **35**, 3446–3464 (2014).

24. Agosta, F. *et al.* Resting state fMRI in Alzheimer's disease: beyond the default mode network. *Neurobiol. Aging* **33**, 1564–1578 (2012).
25. Zhao, Q., Lu, H., Metmer, H., Li, W. X. Y. & Lu, J. Evaluating functional connectivity of executive control network and frontoparietal network in Alzheimer's disease. *Brain Res.* **1678**, 262–272 (2018).
26. Zhao, Q. *et al.* Functional segregation of executive control network and frontoparietal network in Alzheimer's disease. *Cortex* **120**, 36–48 (2019).
27. Sridharan, D., Levitin, D. J. & Menon, V. A critical role for the right fronto-insular cortex in switching between central-executive and default-mode networks. *Proc. Natl. Acad. Sci. U. S. A.* **105**, 12569–12574 (2008).
28. Blessing, E. M., Beissner, F., Schumann, A., Brünner, F. & Bär, K.-J. A data-driven approach to mapping cortical and subcortical intrinsic functional connectivity along the longitudinal hippocampal axis. *Hum. Brain Mapp.* **37**, 462–476 (2016).
29. Kawabata, K. *et al.* Functional connector hubs in the cerebellum. *Neuroimage* **257**, 119263 (2022).
30. Bernard, J. A. *et al.* Dissociable functional networks of the human dentate nucleus. *Cereb. Cortex* **24**, 2151–2159 (2014).
31. Alves, P. N. *et al.* An improved neuroanatomical model of the default-mode network reconciles previous neuroimaging and neuropathological findings. *Commun Biol* **2**, 370 (2019).
32. Li, J. *et al.* Mapping the subcortical connectivity of the human default mode network. *Neuroimage* **245**, 118758 (2021).
33. Buckner, R. L., Krienen, F. M., Castellanos, A., Diaz, J. C. & Yeo, B. T. T. The organization of the human cerebellum estimated by intrinsic functional connectivity. *J. Neurophysiol.* **106**, 2322–2345 (2011).
34. Xue, J. *et al.* Altered Directed Functional Connectivity of the Hippocampus in Mild Cognitive Impairment and Alzheimer's Disease: A Resting-State fMRI Study. *Front. Aging Neurosci.* **11**, 326 (2019).
35. Allen, G. *et al.* Reduced hippocampal functional connectivity in Alzheimer disease. *Arch. Neurol.* **64**, 1482–1487 (2007).
36. Seoane, S., van den Heuvel, M., Acebes, Á. & Janssen, N. The subcortical default mode network and Alzheimer's disease: a systematic review and meta-analysis. *Brain Commun* **6**, fcae128 (2024).
37. Tang, F. *et al.* Differences Changes in Cerebellar Functional Connectivity Between Mild Cognitive Impairment and Alzheimer's Disease: A Seed-Based Approach. *Front. Neurol.* **12**, 645171 (2021).
38. Yao, H. *et al.* Decreased functional connectivity of the amygdala in Alzheimer's disease revealed by resting-state fMRI. *Eur. J. Radiol.* **82**, 1531–1538 (2013).
39. Zhou, B. *et al.* Impaired functional connectivity of the thalamus in Alzheimer's disease and mild cognitive impairment: a resting-state fMRI study. *Curr. Alzheimer Res.* **10**, 754–766 (2013).
40. Westlye, E. T., Lundervold, A., Rootwelt, H., Lundervold, A. J. & Westlye, L. T. Increased hippocampal default mode synchronization during rest in middle-aged and elderly APOE ε4 carriers: relationships with memory performance. *J. Neurosci.* **31**, 7775–7783 (2011).
41. Cabral, J., Kringelbach, M. L., & Deco, G. Functional connectivity dynamically evolves on multiple time-scales over a static structural connectome: Models and mechanisms. *Neuroimage* **160**, 84–96 (2017).
42. Beckett, L. A. *et al.* The Alzheimer's Disease Neuroimaging Initiative phase 2: Increasing the length, breadth, and depth of our understanding. *Alzheimers. Dement.* **11**, 823–831 (2015).
43. Yeo, B. T. T. *et al.* The organization of the human cerebral cortex estimated by intrinsic functional connectivity. *J. Neurophysiol.* **106**, 1125–1165 (2011).
44. Ogawa, S., Lee, T. M., Kay, A. R. & Tank, D. W. Brain magnetic resonance imaging with contrast dependent on blood oxygenation. *Proc. Natl. Acad. Sci. U. S. A.* **87**, 9868–9872 (1990).
45. McKenna, F., Koo, B.-B., Killiany, R. & Alzheimer's Disease Neuroimaging Initiative. Comparison of ApoE-related brain connectivity differences in early MCI and normal aging populations: an fMRI study. *Brain Imaging Behav.* **10**, 970–983 (2016).
46. Ahmadi, H., Fatemizadeh, E. & Motie-Nasrabadi, A. Identifying brain functional connectivity

alterations during different stages of Alzheimer's disease. *Int. J. Neurosci.* **132**, 1005–1013 (2022).
47. Han, F., Liu, X., Mailman, R. B., Huang, X. & Liu, X. Resting-state global brain activity affects early β-amyloid accumulation in default mode network. *Nat. Commun.* **14**, 7788 (2023).
48. Zheng, W., Liu, X., Song, H., Li, K. & Wang, Z. Altered Functional Connectivity of Cognitive-Related Cerebellar Subregions in Alzheimer's Disease. *Front. Aging Neurosci.* **9**, 143 (2017).
49. Uddin, L. Q. *et al.* Controversies and progress on standardization of large-scale brain network nomenclature. *Netw. Neurosci.* **7**, 864–905 (2023).
50. Figueroa, C. A. *et al.* Altered ability to access a clinically relevant control network in patients remitted from major depressive disorder. *Hum. Brain Mapp.* **40**, 2771–2786 (2019).
51. Farinha, M., Amado, C., Morgado, P. & Cabral, J. Increased Excursions to Functional Networks in Schizophrenia in the Absence of Task. *Front. Neurosci.* **16**, 821179 (2022).
52. Caetano, I. *et al.* Perceived stress modulates the activity between the amygdala and the cortex. *Mol. Psychiatry* **27**, 4939–4947 (2022).
53. Dowdle, L. T. *et al.* Statistical power or more precise insights into neuro-temporal dynamics? Assessing the benefits of rapid temporal sampling in fMRI. *Prog. Neurobiol.* **207**, 102171 (2021).
54. Palmer, W. C., Park, S. M. & Levendovszky, S. R. Brain state transition analysis using ultra-fast fMRI differentiates MCI from cognitively normal controls. *Front. Neurosci.* **16**, 975305 (2022).
55. Pang, J. C. *et al.* Geometric constraints on human brain function. *Nature* **618**, 566–574 (2023).
56. MacDonald, M. E. & Pike, G. B. MRI of healthy brain aging: A review. *NMR Biomed.* **34**, e4564 (2021).
57. Bennett, D. A. *et al.* Neuropathology of older persons without cognitive impairment from two community-based studies. *Neurology* **66**, 1837–1844 (2006).
58. Knopman, D. S. *et al.* Neuropathology of cognitively normal elderly. *J. Neuropathol. Exp. Neurol.* **62**, 1087–1095 (2003).
59. Dubois, B. *et al.* Revising the definition of Alzheimer's disease: a new lexicon. *Lancet Neurol.* **9**, 1118–1127 (2010).
60. Dubois, B. *et al.* Research criteria for the diagnosis of Alzheimer's disease: revising the NINCDS-ADRDA criteria. *Lancet Neurol.* **6**, 734–746 (2007).
61. Llano, D. A., Kwok, S. S., Devanarayan, V. & The Alzheimer's Disease Neuroimaging Initiative (ADNI). Reported Hearing Loss in Alzheimer's Disease Is Associated With Loss of Brainstem and Cerebellar Volume. *Front. Hum. Neurosci.* **15**, 739754 (2021).
62. Crane, P. K. *et al.* Development and assessment of a composite score for memory in the Alzheimer's Disease Neuroimaging Initiative (ADNI). *Brain Imaging Behav* **6**, 502–516 (2012).
63. Gibbons, L. E. *et al.* A composite score for executive functioning, validated in Alzheimer's Disease Neuroimaging Initiative (ADNI) participants with baseline mild cognitive impairment. *Brain Imaging Behav* **6**, 517–527 (2012).
64. Nieto-Castanon, A. *Handbook of Functional Connectivity Magnetic Resonance Imaging Methods in CONN.* (Hilbert Press, 2020).
65. Nieto-Castanon, A. *CONN Functional Connectivity Toolbox: RRID SCR_009550, Release 21.* (Hilbert Press, 2021).
66. Andersson, J. L. R., Hutton, C., Ashburner, J., Turner, R. & Friston, K. Modeling Geometric Deformations in EPI Time Series. *NeuroImage* **13**, 903–919 (2001).
67. Ashburner, J. & Friston, K. J. Unified segmentation. *Neuroimage* **26**, 839–851 (2005).
68. Biswal, B., Yetkin, F. Z., Haughton, V. M. & Hyde, J. S. Functional connectivity in the motor cortex of resting human brain using echo-planar MRI. *Magn. Reson. Med.* **34**, 537–541 (1995).
69. Cordes, D. *et al.* Frequencies contributing to functional connectivity in the cerebral cortex in 'resting-state' data. *AJNR Am J Neuroradiol* **22**, 1326–1333 (2001).
70. Vohryzek, J., Deco, G., Cessac, B., Kringelbach, M. L. & Cabral, J. Ghost Attractors in Spontaneous Brain Activity: Recurrent Excursions Into Functionally-Relevant BOLD Phase-Locking States. *Front. Syst. Neurosci.* **14**, 518364 (2020).
71. Eraifej, J. *et al.* Modulation of limbic resting-state networks by subthalamic nucleus deep brain stimulation. *Netw Neurosci* **7**, 478–495 (2023).
72. Stark, E. A. *et al.* The Power of Smiling: The Adult Brain Networks Underlying Learned Infant

Emotionality. *Cereb Cortex* **30**, 2019–2029 (2020).

73. Larabi, D. I. *et al.* Trait self-reflectiveness relates to time-varying dynamics of resting state functional connectivity and underlying structural connectomes: Role of the default mode network. *Neuroimage* **219**, 116896 (2020).